Università degli Studi di Cagliari

PHD DEGREE

International Ph.D. in Innovation Sciences and Technologies

Cycle XXXI

TITLE OF THE PHD THESIS

Fabrication of Cu-based metal matrix composites reinforced with carbon nanofillers

Scientific Disciplinary Sector(s)

ING-IND/22

PhD Student:	Barbara Lasio
Coordinator of the PhD Programme	Prof. Roberto Orrù
Supervisor	Prof. Francesco Delogu

Final exam. Academic Year 2017 – 2018

Thesis defence: January-February 2019 Session

This thesis is dedicated to

Franco and my parents

for all of their lovely support

Table of contents

1. Introduction

In recent times, a deep consciousness of the strict relationship between energy, environment, economy and security issues has progressively grown across the entire world. The local and the global crises of distinct nature have clearly demonstrated that the life in a modern country strongly depends on easily and affordable supply of materials. Various factors, such as the rapid growth of new markets, the development of new materials and technologies and the needs to find very specific properties for new high-tech applications have heavily reduced the availability of raw materials [1–3]. Presently, the resources of most developed countries are not sufficient for sustaining industrial production, economy and competitiveness. Hence, the common practice is to import them from the raw material-rich countries [4].

However, these resource-rich countries have reduced their exports by applying protectionist policies, in order to protect their national industries. Thus, the export reduction and the increasing taxation of specific raw material, pose a severe threat to the global industrial production [5–7]. A symbolic example is of rare earth minerals that are utilized in modern high-tech technology, and whose world market is mainly controlled by China [7–10].

Obviously, this represents a serious risk for those countries that want to maintain or to improve the quality of life, but have deal with the limited resources [11]. This is particularly true for the so called critical raw materials (CRMs), i.e. materials that are especially difficult to obtain due to the reduction of available resources, high costs, political instability in supplier countries, and reduced exportation from the producer.

1.1 Critical Raw Materials

A raw material is classified as a CRM on the basis of various indicators that are related to economic and availability aspects of the resource. In particular, two of the most important parameters to be taken into account are the economic importance (EI) and the supply risk (SR). A raw material is defined as being critical if both dimensions overcome a given threshold.

The EI is related to the potential consequences in the event of an inadequate supply of the raw material and is calculated employing the following equation:

$$EI = \sum_{s} (A_s * Q_s)$$

In the above formula, A_s represents the share of demand of a raw material in a mega sector, where Q_s is the mega sector's Gross Value Added [11].

On the other hand, the parameter SR, depends on the risk of an interruption in the EU supply of the material and examines the concentration of primary supply from raw materials producing countries, considering the trade aspects and the governance performance. The supply risk is calculated using the equation below:

$$SR = HHI_{WGI} * (1 - E_o L_{RIR}) * SI$$

In this formula, SR stands for supply risk; HHI is the Herfindahl Hirschman Index (used as a proxy for country concentration); WGI is the scaled World Governance Index (used as a proxy for country governance); $E_O L_{RIR}$ is the End-of-Life Recycling Input Rate; and SI is the Substitution Index [11].

The raw materials in function of EI and SR are shown in Figure 1. In particular, CRMs are located in the area defined by values of SR ≥ 1 and EI ≥ 2.8 in the graph, and are marked by red dots.

Here, it is worth noting that CRMs are not so weird or unusual. Indeed, although they comprise rare earth metals, CRMs also include relatively common elements like Mg, Co, W, which are present in objects and devices used every day.

Since 2011, the European commission created a list of potential CRMs, which is periodically reviewed and updated. In the last revision conducted in 2017, 78 raw elements that are likely to be critical (58 individual materials and 3 material groups: LRREs, HRREs, PGMs) were recognised. Among them, 27 were classified as CRMs, as shown in Table 1 [7].

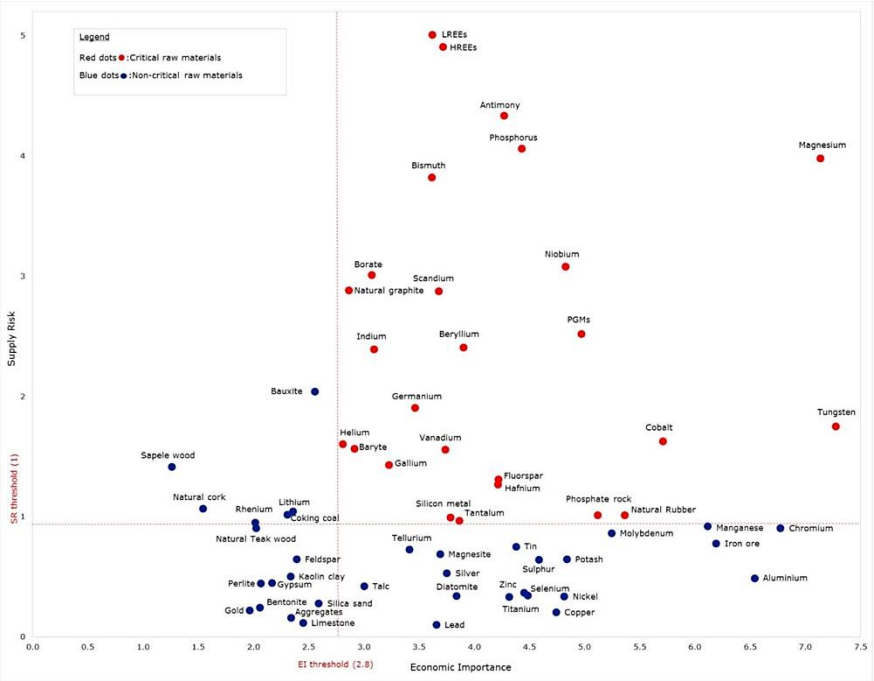

Fig.1 Supply risk and economic importance of raw materials. The red dots represent CRMs, while in blue the non-critical materials [12].

Tab 1. List of CRMs listed in 2017 [13].

CRMs			
Antimony	Fluorspar	Indium	Phosphorus
Baryte	Gallium	Magnesium	Scandium
Beryllium	Germanium	Cobalt	Vanadium
Coking coal	Phosphate rock	Natural graphite	Silicon metal
Borate	Helium	Niobium	Tungsten
Bismuth	Hafnium	Natural rubber	Tantalum
LREEs light rare earth elements	HREEs heavy rare earth elements	PGMs platinum group metals	

The list of CRMs can help the European industries to raise the awareness in developing strategies towards sustainable growth. Furthermore, another aim is to stimulate the increase of competitiveness of EU industry for the production of supply by enhancing new mining and recycling activities, and also improve an efficient use of raw materials.

The major suppliers of CRMs on a global scale are shown in Figure 2, while in Figure 3 the main suppliers to EU.

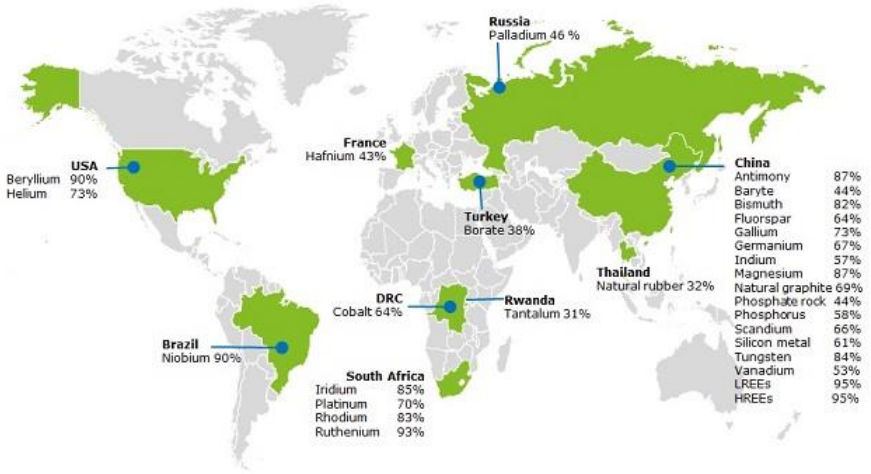

Fig. 2 Global supplier of CRMs [13].

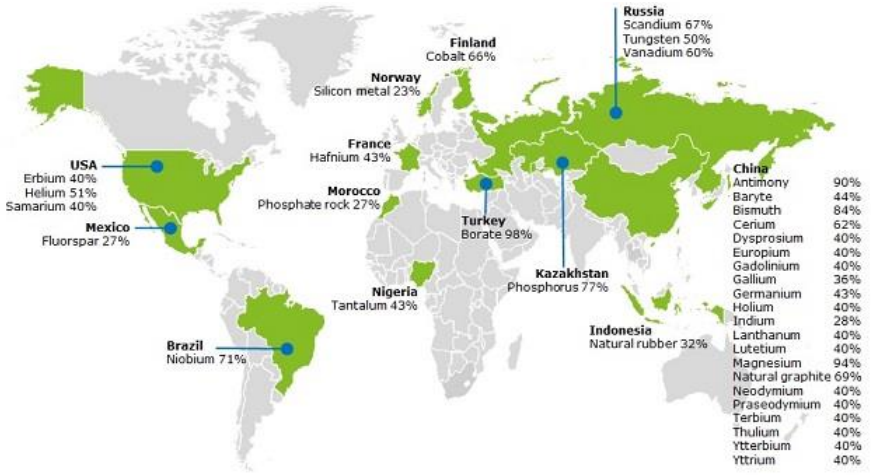

Fig. 3 European supplier of CRMs [13].

From Figures 2 and 3, it is evident that China is the largest producer of CRMs (LRREs, HREEs, Mg, Sb, W) providing up to 70% to the global and 60% to European industrial production. However, other countries such as Brazil (Nb), USA (Be and He), Russia (Pd) and South Africa (Ir, Pt, Rh and Ru) are also significant producers of CRMs. While, it is evident that EU countries have to face with a lack of resources in terms of CRMs.

On the other side, the demand of CRMs in widespread devices is destined to increase with time. For instance, a typical smartphone contains up to sixty elements from the periodic

table, many of which are recognised as critical or potentially critical. Similarly, in the 1980s computer chips contained 11 mineral-derived elements, whose number increased to 15 during the 1990s. Thus, according to this trend, in the coming future the devices would contain as many as 50–60 elements [14].

An obvious solution to overcome the scarcity of CRMs is by substituting them with other abundant elements, along with development of strategies for their efficient use [15].

In this regard, EU is currently financing various actions focused on CRMs within the 7-years platform Horizon 2020, through the European Innovation Partnership (EIP) and the European Cooperation in Science and Technology (COST).

In particular, the EIP promotes both technological and non-technological innovation along the entire chain of raw materials (for knowledge, exploration, licensing, extraction, processing, refining, re-use, recycling, substitution), involving stakeholders from relevant sectors [13]. The EIP also contributes to the objectives of the Commission's flagship initiatives as Innovation Union and Resource Efficient Europe.

The COST is the European framework that support cooperation between researchers, engineers and scholars. The aim is devoted to develop new scientific concepts and products. COST through the "actions" provides resources to create networks of scientists and researchers across Europe.

In this respect, University of Cagliari actively participated as a member of EIP and as a proposer of the Cost Action "Solutions for Critical Raw Materials Under Extreme Conditions (CRM-EXTREME)".

In particular, the "CRM-EXTREME" action is focused on the substitution of CRMs, like Cr, Co, Nb, W, Y, by finding new metal matrix composites or high value alloys. These new materials with enhanced properties of resistance could allow to work under extreme conditions of temperature, loading, friction, wear, corrosion, in energy, transportation and machinery manufacturing industries. Through this action a network of experts has been built in multiscale modelling, synthesis, characterization, engineering design and recycling to find alternatives to the use of CRMs and to promote the industrial production of substituted materials.

This thesis is inspired by the above-mentioned problems regarding the shortage of CRMs and the research activity is carried out within the framework of the CRM-EXTREME action. The research work focuses on composite structural material and, in particular, on the production of Cu-matrix composites (Cu-MCs) reinforced with carbon nanofillers. This choice emerged from the appealing properties of Cu-MCs, such as the unique

combination of thermal and electric conductivities, self-lubricating properties of graphite, cost-effectiveness and availability. For all these reasons, such composite materials can be attractive for a broad spectrum of industrial applications.

Bibliography

[1] D. Rosenau-Tornow, M. Buchholz, P., Riemann, A., Wagner, Assessing the long-term supply risks for mineral raw materials — a combined evaluation of past and future trends., Resour.Policy. 34 (2009) 161–175.

[2] F. Krausmann, F.-K. Gingrich, S., Eisenmenger, N., Erb, K.-H., Haberl, H., M., Growth in global materials use, GDP and population during the 20th Century., Ecol. Econ. (2009) 2696–2705.

[3] Greenfield, A., T.E. Graedel, The omnivorous diet of modern technology., Resour. Conserv. Recycl. 74 (2013) 1–7.

[4] A. Behrens, S. Giljum, S., Kovanda, J., Niza, The material basis of the global economy: worldwide patterns of natural resource extraction and their implications for sustainable resource use policies., Ecol.Econ.64(2),444–453, Spec. Sect. Agric. (2007).

[5] C. Parthemore, Elements of Security: Mitigating the Risks of U.S. Dependence on Critical Minerals. Center for a New American Security, WashingtonDC., 2011.

[6] G.A. Campbell, Rare earth metals: a strategic concern., Miner.Econ. 27 (2014) 21–31.

[7] S. Massari, M. Ruberti, Rare earth elements as critical raw materials : Focus on international markets and future strategies, Resour. Policy. 38 (2013) 36–43. doi:10.1016/j.resourpol.2012.07.001.

[8] D.J. Kingsnorth, The Challenges of Meeting Rare Earths Demand in2015., in: Proc. Technol. Rare Earth Met. Policy Conf. Washington, DC, March17., 2010.

[9] L. Corporation, Chinese Rare Earth Export Quota Significantly Reduced for Second Half 2010, (2011).

[10] T. Keller, Chinese rare earths supply squeeze doomed. The Globe and Mail, April 28., (2011).

[11] G.A. Blengini, P. Nuss, J. Dewulf, V. Nita, L.T. Peirò, B. Vidal-Legaz, C. Latunussa, L. Mancini, D. Blagoeva, D. Pennington, M. Pellegrini, A. Van

Maercke, S. Solar, M. Grohol, C. Ciupagea, EU methodology for critical raw materials assessment: Policy needs and proposed solutions for incremental improvements, Resour. Policy. 53 (2017) 12–19. doi:10.1016/j.resourpol.2017.05.008.

[12] European Commission, Study on the review of the list of critical raw materials Final report, (2017).

[13] ec.europa.eu, (n.d.) https://ec.europa.eu/growth/sectors/raw-materials/.

[14] R.G. Eggert, Minerals go critical, Nat. Publ. Gr. 3 (2011) 688–691. doi:10.1038/nchem.1116.

[15] A.H. Tkaczyk, A. Bartl, A. Amato, V. Lapkovskis, M. Petranikova, Sustainability evaluation of essential critical raw materials : cobalt , niobium , tungsten and rare earth elements, (2018).

2. Scientific aspects

2.1 Composite materials

A composite is a combination of two or more materials that exhibit improved or different properties with respect to the individual components used alone. One of the constituents is the matrix in which the reinforcements are dispersed. The constituents can be constituted of any material such as metal, polymer, ceramic, carbon etc. The material of the matrix also assigns a classification of the type of composites [1].

The properties of the composite are linked to the composition, type or shape of the reinforcement and the methodologies of preparation [2].

The reinforcements can have different shape such as fibrous, laminar or granular. The fibres into the composite can be continuous or discontinuous depending on their length and can have a preferential orientation or be randomly arranged [3].

In laminar reinforced composites, the layers of materials are held together with the matrix, in a sandwich like structure. For this particular reinforcement and also for the fibres, the properties of the composite and in particular the mechanical properties depend on the direction of the applied stress that must be orthogonal with respect to the filler's orientation.

In the case of particulate composites, the filler is constituted of particles embedded in the matrix. The particles can be in the form of flakes or powder [3,4]. This material shows isotropic properties when the filler is homogeneously distributed in the matrix.

Nowadays, the composites find their utilization in several industrial productions ranging from simple objects to advanced performing devices [5]. They are involved in a wide spectrum of sectors like aerospace, automotive, energy and biomedicine. Furthermore, composites, are also used in industries equipment for processes that requires resistance to high-temperature, corrosion, oxidation, and wear [6].

Among all the various fields of application of composite materials, this thesis is aimed to the structural application. The materials characterised by these properties are detailed below.

2.1.2 Structural materials

Structural materials are materials that have to sustain and resist loads. They are applied in various fields such as transportation, construction, energy generation, and many other industrial sectors. In particular composites are optimal structural materials.

For structural applications the material essentially must have good mechanical performances in terms of hardness, strength, stiffness, ductility, toughness (energy absorbed in fracture) and vibration damping ability [2].

A clarifying example in the construction sector, may be the materials involved in a building. The parts of a building can have different purpose, for instance, the steel is used to reinforce the columns that bear the loads of all the structure, while the concrete architectural panel covers the face of the building. All these parts are structural materials, but only the columns sustain the load. The mechanical strength and stiffness are essentially in the case of the columns [2].

The structural materials can be tailored according to the required application. For instance, in fields of applications that require resistance to corrosion, high temperature and thermal cycling [2].

Structural materials are made of metal, cement and polymer, but also carbon and ceramic materials that are optimal for high-temperature applications [2].

Some common structural materials made from metals are steel and Al alloys. Steel is advantageous because of its high strength, while Al for its low density.

On the other hand, the use of metal matrix composites are much more favourable for the good properties achieved in terms of modulus, creep resistance, and low thermal expansion coefficient with respect to their corresponding metal [2].

2.2 Metal matrix composites (MMCs)

MMCs are increasingly replacing a number of conventional structural materials in the automotive, aerospace and sports industries, driven by the demand for lightweight and higher-strength components [4,7–14]. The properties of MMCs can be designed based on the required material and depending on the application.

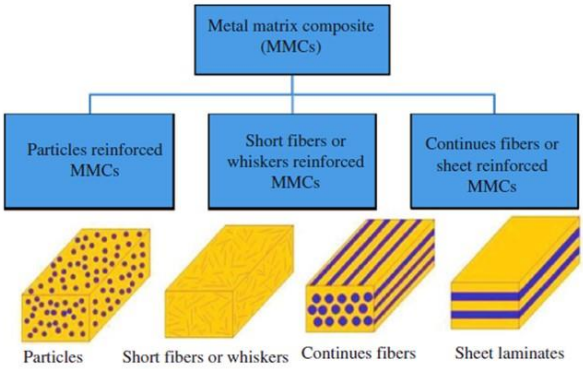

Fig. 1 Classification of MMCs based on reinforcing material structure [15].

Based on the form of the reinforcement MMCs can be classified into particle-reinforced, short fibres, continuous fibres or laminate MMCs [7], as shown in Figure 1.

Continuous fibres' reinforcement provides the most effective strengthening (in a given direction). Particle reinforced materials are more attractive due to their cost-effectiveness, isotropic properties, and their ability to be processed using technology similar to the one used for monolithic materials. Short fibres' reinforcement, which are randomly oriented, also have better isotropic properties than continuously reinforced composites, due to the lower aspect ratio and more random orientation of the reinforcements. Moreover, they can be fabricated using processing techniques similar to those commonly used for unreinforced matrix materials [16].

In MMCs, the metal matrix contributes to the ductility and toughness, whereas reinforcements provide stiffness, strength and wear properties. The most widespread matrices have as elements Al, Mg, Fe, Ni, Ti, and Cu [17–28].

Another parameter to be taken into consideration is the compatibility between the matrix material and the reinforcement. The reaction between the matrix and reinforcement can form intermetallic compounds at the interface, which may cause the unwanted and dangerous effect of transferring load to the reinforcements. Furthermore, the reaction products may act as sites for nucleation of cracks [16].

2.2.2 Fabrication methods of MMCs

The selection of the processing route depends on many factors including type and level of reinforcement loading and the degree of microstructural integrity desired [29].

In ex situ preparation, the reinforcement materials are prepared separately before the composite fabrication and are thereafter incorporated into the host metal matrix without any reaction between the reinforcing materials and the host matrix [14,30]. In the case of in situ preparation, the reinforcing phases are formed during the fabrication of the metal by the reaction between the precursor materials used [13,31].

MMCs fabrication techniques can also be grouped into liquid state and solid-state methods.

The liquid methods of fabrication involve, in general, the incorporation of dispersed phase into a molten metal matrix and the subsequent solidification. In this manner a good interfacial bonding between the matrix and the dispersed phase can be obtained to achieve enhanced mechanical properties of the composites [32]. The examples of the liquid state processes are stir casting, infiltration, disintegrated melt deposition and pressure infiltration.

In solid-state methods, MMCs are generally formed in situ, as a result of the mutual dispersion of bonding metal matrix and dispersed phase. This mutual diffusion in solid state happens between matrix and reinforcements at high temperature and under pressure. Examples of solid state MMCs fabrication methods are: diffusion bonding and powder metallurgy [32].

Fabrication by liquid state and casting methodology is performed through blending of reinforcing elements, such as dispersion of particles and short fibres in molten alloy matrix [33–35]. In this case, the wettability of the reinforcements in the molten metal is important. To increase the wettability of the MMCs constituents, the reinforcement particles can be covered with layers of other material. In the case of A356 Al alloy reinforced with graphite, the particles were modified by layers of Ni to improve the mutual wettability [34].

The liquid infiltration technique consists of the process in which the melted metal is infiltrated through the pores of a preformed dispersed phase [36]. There are two types of infiltration techniques, direct squeeze casting and indirect squeeze casting of preliminary heated preforms, which are represented schematically in Figure 2.

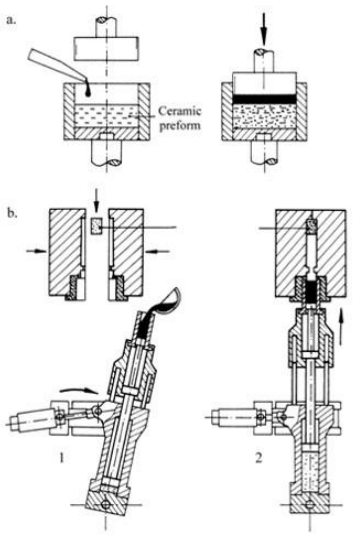

Fig. 2 Infiltration production techniques by cast composite materials through (a) direct squeeze casting method and (b) indirect squeeze casting method [37].

The solid method of fabrication by diffusion bonding consists of a process where a matrix in the form of foils and a dispersed phase, such as fibres, is stacked in order and then pressed at high temperature. The results of this process are MMCs laminate with a multilayer structure [32].

The powder metallurgy method is an important group for the production of composite materials. Such method is based on blending of matrix powders and reinforcing elements (powders, platelets and ceramic fibres) and further cold pressing in a desired shape and sintering followed by plastic working (forging, extrusion) [29]. Typical powder metallurgy processing is shown in Figure 3. The powder metallurgy consists of some basic steps; powder manufacture, powder mixing and blending, compacting and sintering. Mechanical alloying is a widely applied method for the production of composite powders, characterised by very fine grains. Some examples of composites prepared by mechanical alloying are with Mg, Al, and Cu matrix [15,26,33,38].

The process is performed by a high energy ball mill (BM), which allows the dispersion of hard reinforcements in to a relatively soft metal matrix [37]. The dispersed reinforcement in fine matrix can be obtained through the high energy impacts and high frequency from colliding balls to the premixed powders in a mill vial. During the milling the repeated severe deformation, welding and fragmentation allow the refinement of the material [39–41]. The composite powder processed by BM can then be pressed and consolidated by hot plastic working like extrusion, forging or hot isostatic pressing, sintered and cold plastic worked [39,43].

Compaction step is generally performed at room temperature, while the sintering process is usually conducted at high temperature and atmospheric pressure [29]. This fabrication method is advantageous due to its capability of incorporating a relatively high-volume fraction of filler and fabricating composites with matrix alloy and reinforcement systems that are otherwise immiscible by liquid casting [29].

The mechanical properties of the material can be tailored through the control of the starting components and process parameters. Also, the properties can be improved through the secondary processing operations like the thermal treatments or the sintering steps.

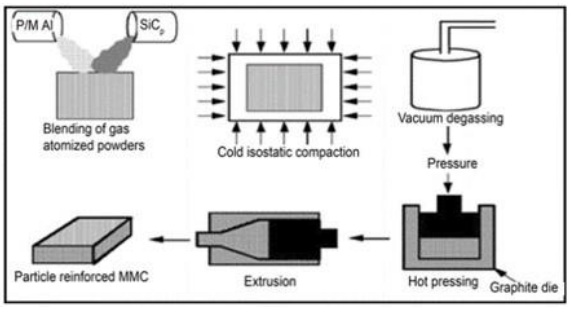

Fig. 3 Typical powder metallurgy processing [42].

2.3 Carbon nanofillers reinforced Cu-MCs

Among the different MMCs, Cu-MCs reinforced by carbon nanofiller are attractive materials. Cu-MCs combines the electrical and thermal conductivities, ductility and corrosion resistance of the matrix with the high thermal and electrical properties of the filler [43].

These composites are widely used in many industrial applications, such as brushes, contact strips, and structural materials [44–47].

Several carbon nanofillers have been used as reinforcement in a copper matrix, such us graphite [48], carbon nanotubes [49–51], graphene [50,52–54], graphite nanoplatelets [55], and nano-diamonds [56].

Uniform dispersions of carbon nanofillers within the metal matrices are usually difficult. Several studies showed that carbon nanoparticles have a strong tendency to agglomerate due to the large surface area and to the Van der Waals forces between carbon atoms. For instance, 0.5 vol % of graphite nanoplatelets strongly agglomerated in a Cu-matrix [57].

However, many different processes have been developed to improve the dispersion capability, such as molecular-level mixing [48,58], ball milling [59], electroless plating [57] or surface modification of carbon fillers and Cu powder by polymers before mixing and sintering [60].

2.4 Aim of the work

One issue of a great interest in this field is the development of an optimal fabrication methodology to obtain good properties in the material. This has, also, to consider the production of materials with a series of tailored physical and chemical properties and the possibility to scaling up to a level of an industrial production. In particular, it is true in the case of metal matrix composites reinforced with carbon nanofillers, where the interaction between the components affects the dispersion. In fact, the strong tendency of aggregation typical of the carbon nanofillers alters the homogeneous distribution into the matrix.

Due to these strong interactions the methodologies of deformation and agitation are usually inadequate. Even if a long duration time of mixing is performed to distribute the components, a large amount of aggregates of dispersoids are still present into the matrix. These large dispersoids alter negatively the properties of the final material. In particular, the presence of aggregate of carbon nanofillers into the matrix, not homogeneously distributed, can make the material weak in the case of moderate stress.

Typical is the case of mechanical processing by ball milling. Ball milling is born precisely for the dispersion of one phase into another, but in some cases can result to be inefficient. For instance, in the case of milling of two phase with different hardness an optimal dispersion is extremely difficult. Although ball milling is a relevant fabrication method, also easily applicable and scalable to industrial production, currently does not warrant the necessary standard to achieve success for this step.

The critical issues in the use of ball milling lies in the apparent inability of forced mixing at the microscopic level. The efficiency of mixing and dispersion are far from those typical of the metallurgical process. In these methodologies, the hard and refractory dispersoids are homogeneously distributed in the molten metal matrix. Therefore, a possible strategy to use ball milling on an industrial scale to produce metal composites

with carbon nanofillers is to improve efficiency of dispersion up to the level of the process in the molten phases.

Despite this goal seems difficult to achieve, it should be noted that the recent literature suggests that a possible solution can stem from the combination of methodologies that involve severe mechanical deformation and high temperature thermal treatments. The mechanical treatment, in principle, favours a remarkably good dispersion of the reinforcement into the matrix allowing the mixing of the phases, while the thermal treatments help the incorporation on the microscopic level. In particular, in the case of carbon-based nanofillers the thermal treatment is necessary to avoid the preferential distribution on the grain boundary that is detrimental for the mechanical properties. This effect can be contrasted by the repeated mechanical deformation on the thermal treated materials. In fact, the thermal treatment can promote the grain growth processes, thereby allowing the inclusion of the carbon-based nanofiller into relatively large grains. In this way, the subsequent mechanical processing allows the refinement of the grain without the preferential mechanism of grain boundary sliding at work.

This thesis is inspired from the above-mentioned considerations. The idea is that, the appropriate combination of mechanical and thermal treatments can allow to achieve an optimal fine and homogeneous dispersion of the reinforcement into the metal matrix. Then the powders of metal together with the dispersoids could be processed by BM and subsequently thermally treated to achieve a homogeneous distribution and the incorporation into the grain of the matrix.

Starting from the evidences shown in literature the thesis was focused on the fabrication of MMCs with the copper matrix and reinforced by carbon nanofillers such as graphite and graphene. Such type of carbon nanofillers could be a suitable alternative to the use of CRMs as dispersoids in the conventional materials. Graphite is an economic and viable source of carbon that can help reducing the use of CRMs. Graphene is an efficient dispersoid that has high mechanical properties when distributed homogeneously into the matrix.

The ultimate objective of the research work, is the definition of a methodology of fabrication, which through the optimization and the combination of the mechanical and the thermal treatments would allow to obtain MMCs with carbon nanofillers and with high mechanical performances.

Finally, to compare with the previous, another method of dispersion is also been tested, the molecular-level mixing. This novel methodology, through the chemical reaction of

the precursor of Cu in presence of the carbon nanofillers, can achieve a homogeneous distribution of the reinforcements into the metal matrix, and also allows obtaining good mechanical properties of the composite.

Bibliography

[1] E.B. Sebok, R.L. Taylo, Concise Encyclopedia of Composite Materials, 2007. doi:10.1017/CBO9781107415324.004.

[2] D.D.L. Chung, Applied Materials Science, 2001. doi:10.1201/9781420040975.

[3] Classification of composites, (n.d.). http://nptel.ac.in/courses/Webcourse-contents/IISc-BANG/Composite Materials/pdf/Lecture_Notes/LNm1.pdf.

[4] K.K. Chawla, Composite Materials Science and Engineering, 1985. doi:10.1177/0892705714554493.

[5] lucas barcelos otani, H. Alves, sandro campos Amico, Elastic moduli characterization of composites using the impulse excitation technique, Tech. Rep. (2014).

[6] Carl Zweben, Composite Materials, in: Mech. Eng. Handbook, M. Kutz (Ed.)., 2015. doi:https://doi.org/10.1002/9781118985960.meh110.

[7] N. Chawla, Metal Matrix Composites, 2006. doi:10.1007/b101197.

[8] J.M. Kunze, C.C. Bampton, Challenges to developing and producing MMCs for space applications, Jom. 53 (2001) 22–25. doi:10.1007/s11837-001-0141-5.

[9] Pradeep Rohatgi, Cast aluminum-matrix composites for automotive applications, JOM. 43 (1991) 10–15. doi.org/10.1007/BF03220538.

[10] P.K. Rohatgi, D. Weiss, N. Gupta, Applications of fly ash in synthesizing low-cost MMCs for automotive and other applications, JOM. (2006). doi:10.1007/s11837-006-0232-4.

[11] Shelley, J. S.; Leclaire, R.; Nichols, Metal-matrix composites for liquid rocket engines, Jom. 53 (2001) 18–21. %0A10.1007/s11837-001-0140-6.

[12] and A.T. T. Suganuma, Application of Metal Matrix Composites to Diesel Engine Pistons, J. Iron Steel Inst. Jpn. 75 (1989). doi:http://dx.doi.org/10.2355/tetsutohagane1955.75.9_1790.

[13] T.W. Clyne, P.J. Withers, An Introduction to Metal Matrix composites, (n.d.).

[14] B. Maruyama, W.H.H. Jr., Discontinuously Reinforced Aluminum: Current Status

and Future Direction, J. Miner. Met. Mater. Soc. (1999) 59–61. doi:10.1007/s11837-999-0225-1.

[15] J.M. Mistry, P.P. Gohil, Research review of diversified reinforcement on aluminum metal matrix composites : fabrication processes and mechanical characterization, De Gruyter. (2017) 1–15. doi:10.1515/secm-2016-0278.

[16] A.B. Pandey, Metallic Matrices, ASM Int. Handb. (2001) 380–382.

[17] A. Azarniya, H.R. Madaah Hosseini, A new method for fabrication of in situ Al/Al 3 Ti–Al 2 O 3 nanocomposites based on thermal decomposition of nanostructured tialite, J. Alloys Compd. (2015). doi:10.1016/j.jallcom.2015.04.145.

[18] A. Azarniya, H.R.M. Hosseini, M. Jafari, N. Bagheri, Thermal decomposition of nanostructured Aluminum Titanate in an active Al matrix: A novel approach to fabrication of in situ Al/Al2O3-Al3Ti composites, Mater. Des. (2015). doi:10.1016/j.matdes.2015.09.050.

[19] A. Sha, S.F. Kashani-bozorg, A.P. Gerlich, Strengthening analyses and mechanical assessment of Ti / Al 2 O 3 nano-composites produced by friction stir processing, Mater. Sci. Eng. A. (2015). doi:10.1016/j.msea.2015.02.038.

[20] U.O. Tunçal T, Industrial sludge remediation with photonic treatment using Ti–Ag nano-composite thin films: persistent organic pollutant removal from sludge matrix., J Env. Manag. 149 (2015) 37–45.

[21] T. Varol, A. Canakci, The effect of type and ratio of reinforcement on the synthesis and characterization Cu-based nanocomposites by flake powder metallurgy, J. Alloys Compd. 649 (2015) 1066–1074. doi:10.1016/j.jallcom.2015.07.008.

[22] X. Long, Y. Bai, M. Algarni, Y. Choi, Q. Chen, Study on the strengthening mechanisms of Cu/CNT nano-composites, Mater. Sci. Eng. A. (2015). doi:10.1016/j.msea.2015.08.012.

[23] A. Canakci, T. Varol, Microstructure and properties of AA7075 / Al – SiC composites fabricated using powder metallurgy and hot pressing, Powder Technol. (2014). doi:10.1016/j.powtec.2014.08.016.

[24] A. Dey, K.M. Pandey, Magnesium Metal Matrix Composites - A Review, Rev. Adv. Mater. Sci. (2015).

[25] I.H. Alsohaimi, and A.M.A. mahri Moonis Ali Khan, Zeid Abdullah Alothman, Mohammad Rizwan Khan, Mahendra Kumar1, Synthesis, characterization, and application of Fe-CNTs nanocomposite for BrO3- remediation from water samples, J Ind Eng Chem 2015;26218–25. 26 (2015) 218–25.

[26] C. Suryanarayana, N. Al-Aqeeli, Mechanically alloyed nanocomposites, Prog. Mater. Sci. 58 (2013) 383–502. doi:10.1016/j.pmatsci.2012.10.001.

[27] B. Gokul, P. Saravanan, V.T.P. Vinod, M. Černík, R. Sathyamoorthy, Synthesis of Ni/NiO nanocomposites by hydrothermal-assisted polyol process and their magnetic properties as a function of annealing temperature, Powder Technol. (2015). doi:10.1016/j.powtec.2015.01.002.

[28] Wang YHe YXiao RLi HAifantis KHuang X, Investigation of crack patterns and cyclic performance of Ti–Si nanocomposite thin film anodes for lithium ion batteries., J Power Sources. 202 (2012) 236–45.

[29] R. Rana, R. Purohit, S. Das, Review of recent Studies in Al matrix composites, Int. J. Sci. Eng. Res. 3 (2012) 1–16. http://www.ijser.org/researchpaper%5CReview-of-recent-Studies-in-Al-matrix-composites.pdf.

[30] H. L. Cox, The elasticity and strength of paper and other fibrous materials, Brit. J. App. Phys. 3 (1952) 122.

[31] J. D. Parker, B. Wilshire, J. D. Parker, B. Wilshire, Met. Sci. J. 9 (1975) 248–252.

[32] R. Anish, G. Robert Singh, M. Sivapragash, Techniques for processing metal matrix composite; A survey, Procedia Eng. 38 (2012) 3846–3854. doi:10.1016/j.proeng.2012.06.441.

[33] S.F. Corbin, D.S. Wilkonson, The tensile properties of a particulate reinforced Al alloy in the temperature range 196±3008C, Canad. Met. Quart. 35 (1996) 189±198.

[34] W. Ames, A.T. Alpas, Wear mechanisms in hybrid composites of graphite-20% SiC in A356 aluminium alloy (Al-7% Si-0.3% Mg), Met. Mater. Trans. A. 26 (1995) 85±98.

[35] S. Skolianos, Mechanical behaviour of cast SiCp reinforced Al± 4.5%Cu±1.5%Mg alloy, Mater. Sci. Eng. A. 210 (1996) 76±82.

[36] A. Mortensen, J.A. Cornie, M.C. Flemings, Columnar dendritic solidification in a metal-matrix composite, Metall. Mater. Trans. A. (1988). doi:10.1007/BF02649285.

[37] J.W. Kaczmar, K. Pietrzak, W. Wlosinski, The production and application of metal matrix composite materials, J. Mater. Process. Technol. 106 (2000) 58–67. doi:doi: 10.1016/S0924-0136(00)00639-7.

[38] H. Yue, L. Yao, X. Gao, S. Zhang, E. Guo, H. Zhang, X. Lin, B. Wang, Effect of ball-milling and graphene contents on the mechanical properties and fracture mechanisms of graphene nanosheets reinforced copper matrix composites, J.

Alloys Compd. 691 (2017) 755–762. doi:10.1016/j.jallcom.2016.08.303.

[39] C. Suryanarayana, Mechanical alloying and milling, Prog. Mater. Sci. 46 (2001) 1–184.

[40] P. Baláž, M. Achimovičová, M. Baláž, P. Billik, Z. Cherkezova-Zheleva, J.M. Criado, F. Delogu, E. Dutková, E. Gaffet, F.J. Gotor, R. Kumar, I. Mitov, T. Rojac, M. Senna, A. Streletskii, K. Wieczorek-Ciurowa, Hallmarks of mechanochemistry: from nanoparticles to technology, Chem. Soc. Rev. 42 (2013) 7571. doi:10.1039/c3cs35468g.

[41] Ismail Ozdemir, Sascha Ahrens, Silke Miicklich, Bernhard Wielage, Nanocrystalline Al-Al2O3p and SiCp composites produced by high energy ball milling, J. Mater. Process. Technol. 205 (2008) 111–118.

[42] D.A. C. Borgonovo, Manufacture of Aluminum Nanocomposites: A Critical Review, Mater. Sci. Forum. 678 (2011).

[43] C.P. Samal, J.S. Parihar, D. Chaira, The effect of milling and sintering techniques on mechanical properties of Cu – graphite metal matrix composite prepared by powder metallurgy route, J. Alloys Compd. 569 (2013) 95–101. doi:10.1016/j.jallcom.2013.03.122.

[44] H. Zhao, L. Liu, Y. Wu, W. Hu, Investigation on wear and corrosion behavior of Cu-graphite composites prepared by electroforming, Compos. Sci. Technol. 67 (2007) 1210–1217. doi:10.1016/j.compscitech.2006.05.013.

[45] R.R. Zahran, I.H.M. Ibrahim, G.H. Sedahmed, The corrosion of graphite/copper composites in different aqueous environments, Mater. Lett. 28 (1996) 237–244. doi:10.1016/0167-577X(94)00095-6.

[46] P.K. Rohatgi, S. Ray, Y. Liu, Tribological properties of metal-matrix-graphite particle composites, Int. Mater. Rev. 37 (1992) 129–149.

[47] J. Kováčik, Š. Emmer, J. Bielek, L. Keleši, Effect of composition on friction coefficient of Cu-graphite composites, Wear. (2008). doi:10.1016/j.wear.2007.11.012.

[48] G.C. Yao, Q.S. Mei, J.Y. Li, C.L. Li, Y. Ma, F. Chen, M. Liu, Cu/C composites with a good combination of hardness and electrical conductivity fabricated from Cu and graphite by accumulative roll-bonding, Mater. Des. 110 (2016) 124–129. doi:10.1016/j.matdes.2016.07.129.

[49] C.Q. Long X, Bai Y, Algarni M, Choi Y, Study on the strengthening mechanisms of Cu/CNT nano-composites., Mater Sci Eng, A. 645 (2015) 347–56.

[50] X. Chen, J. Tao, J. Yi, Y. Liu, C. Li, R. Bao, Strengthening behavior of carbon nanotube-graphene hybrids in copper matrix composites, Mater. Sci. Eng. A. 718 (2018) 427–436. doi:10.1016/j.msea.2018.02.006.

[51] S.H. Daoush,W.M.; Lim, B.K.; Mo, C.B.; Nam, D.H.; Hong, Electrical and mechanical properties of carbon nanotube reinforced copper nanocomposites fabricated by electroless deposition process., Mater. Sci. Eng. A. 513 (2009) 247–253.

[52] W. Li, D. Li, Q. Fu, C. Pan, Conductive enhancement of copper/graphene composites based on high-quality graphene, RSC Adv. 5 (2015) 80428–80433. doi:10.1039/C5RA15189A.

[53] J. Hwang, T. Yoon, S.H. Jin, J. Lee, T.S. Kim, S.H. Hong, S. Jeon, Enhanced mechanical properties of graphene/copper nanocomposites using a molecular-level mixing process, Adv. Mater. 25 (2013) 6724–6729. doi:10.1002/adma.201302495.

[54] F. Chen, J. Ying, Y. Wang, S. Du, Z. Liu, Q. Huang, Effects of graphene content on the microstructure and properties of copper matrix composites, Carbon N. Y. 96 (2016) 836–842. doi:10.1016/j.carbon.2015.10.023.

[55] D. Zhang, Z. Zhan, Strengthening effect of graphene derivatives in copper matrix composite, J. Alloys Compd. 654 (2016) 226–233.

[56] Andrey M.Abyzov, F. M.Shakhov, A.I. .Averkin, V.I. Nikolaev, Mechanical properties of a diamond–copper composite with high thermal conductivity, Mater. Des. 87 (2015) 527–539.

[57] D. Zhang, Z. ; Zhan, Preparation of graphene nanoplatelets–copper composites by a modified semi-powder method and their mechanical properties., J. Alloy. Compd. 658 (2016) 663–671.

[58] D. Berber, S.; Kwon, Y.K.; Tománek, Unusually high thermal conductivity of carbon nanotubes., Phys. Rev. Lett. 84 (2000) 4613–4616.

[59] Y. Chen, X. Zhang, E. Liu, C. He, C. Shi, J. Li, P. Nash, N. Zhao, fabrication of in-situ grown graphene reinforced Cu matrix composites., Sci Rep. 6 (2016) 19363.

[60] Z. Jiang, R.; Zhou, X.; Fang, Q.; Liu, Copper–graphene bulk composites with homogeneous graphene dispersion and enhanced mechanical properties., Mater. Sci. Eng. A. 654 (2016) 124–130.

3. The idea

The strategy that has been adopted for the fabrication of Cu-MC reinforced with carbon-based nanofillers involves an innovative methodology with a combination of ball milling (BM) and spark plasma sintering (SPS).

BM is a simple, economic and scalable technique applied for processing a large amount of product, and is widely used for industrial production [1,2]. Through this technique it is possible to refine the structure, thus allowing the dispersion of the reinforcement into the matrix [1]. The sintering by SPS is a fast and controlled thermal consolidation treatment that produces bulk sample from powders.

The dispersion through BM between different phases is an effective methodology, although it is quite difficult for the obtainment of the forced mixing at the microscopic level. This thesis has tackled this aim and a new methodology has been defined and consists in consecutive steps of grinding and consolidation of the mixed powders, where each successive step starts again from the crushed material. The idea is completed through the controlled thermal treatment achieved by SPS that can increase the grain of Cu and allow the incorporation of graphite.

In the following it is shown that, through the combination of the two techniques, BM and SPS, it can be possible to obtain an optimal fine dispersion of the reinforcements into the matrix to the microscopic level.

Another potential method of dispersion, the molecular level mixing has been performed to compare it with the combination of BM and SPS. In this case, during the redox synthesis to obtain Cu powder it is possible to disperse and incorporate the carbon nanofiller at the atomic level.

These two methodologies are very different considering their starting point, as it is shown in Figure 1.

BM is a top-down approach while molecular level mixing is a bottom-up approach.

Considering the top of the Figure 1, the top-down approach is characterized by the bulk material that is reduced to small part to reach a nanostructure. Instead, on the bottom of the Figure 1, the bottom-up approach is characterized by the atoms and molecules that are assembled to obtain the nanomaterial.

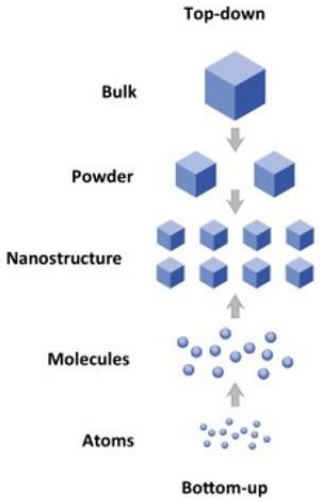

Fig. 1 Scheme of the Top-down and bottom-up approaches in nanotechnology [3].

Accordingly, in a top-down approach, the fabrication of the composite powder starts from the mixture, in various compositions, of micrometrical graphite and Cu, as it is shown on the left in Figure 2. Then the mixture powder is processed with ball milling and then sintered with SPS. In that way, the consecutive combination of the two techniques allows to obtain a composite with a fine and homogeneous dispersion of nano graphite into the grain of the Cu matrix. Through the optimization of the parameters of fabrication, such as composition, milling time and temperature of sintering, it is possible to obtain a Cu-MC reinforced with nano graphite with high mechanical properties.

The second case, the bottom-up route, consists of a chemical reaction of the precursor of Cu in presence of an aqueous dispersion of graphene nanoplatelet, as shown in Figure 2. During the redox reaction, the precipitation of the Cu powder can ensure the incorporation of the graphene into the matrix. By this approach a homogeneous distribution and a microscopic level mixing can be achieved between the dispersoid and the matrix. In this case, the optimal parameters of the reaction have been tested, such as concentration of the precursors, the best dilution of graphene, the right pH and the convenient quantity of product. The composite powder produced has been consolidated by SPS obtaining a Cu-MC with a homogeneous dispersion of graphene into the matrix.

The fabrication methods used in this research work have been described below. The specific characteristics of the methodologies will be elaborated to explain what mechanisms act during the processing of the powders.

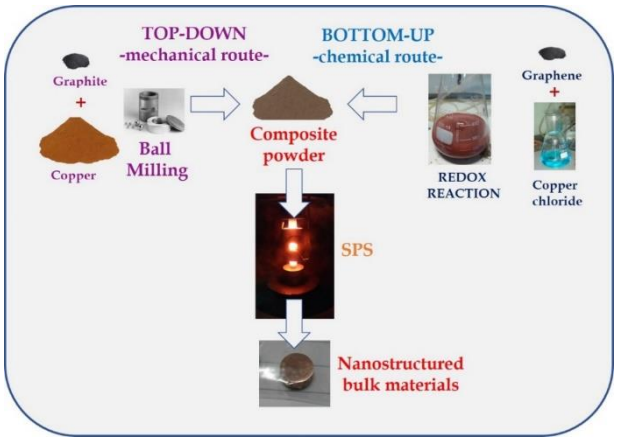

Fig. 2 BM fabrication as top-down approach and chemical synthesis as bottom-up approach.

3.1 Fabrication methodologies

3.1.1 Ball Milling

Generally, in the typical BM process, the reactor is filled partially with powders and milling tools. The collisions between the milling tools in the reactor and the powders transferred energy inputs to the material which induce severe plastic deformation, fracturing and cold welding, which result in a refining of grain size, amorphization, phase transformation and also a forced mixing of different components [1,4–6].

The impacts are a consequence of the movement of the reactor, or a part of it [1,2]. Every collision involves a fraction of the powder which is trapped between the colliding surfaces and subjected to mechanical load [1,4,6]. This process mechanism is shown in Fig. 3.

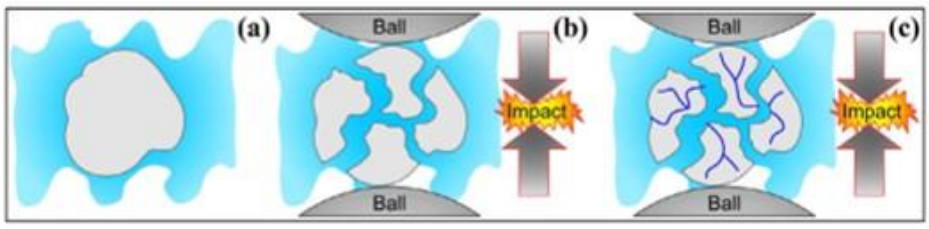

Fig. 3 The schematic mechanism of milling impact: a) the powder is between two colliding surface and fractured by the impact, b) with the proceeding of the process c) an increasing number of fractures and deformations formed [7].

During the process the particles are continuously flattened, cold welded, fractured and rewelded. When there's the collision of two balls, an amount of powder is trapped in between them. An amount of 1000 particles (aggregate weight around 0.2 mg), usually, are trapped during each collision. The impact on the powder particles plastically deforms conducting to hardening and fracture. The formation of new surfaces enables the welding of the particles and this drives to the increase of particle size [8].

At the beginning of the process the particles are soft, in the case of ductile-ductile or ductile-brittle material combination, and there's high tendency to weld together and to form large particles. The wide part of the particles become three times bigger than the starting powders. In this stage there are the formation of a layered composite that consist in a combination of the starting powder [8].

During the continued deformation, the particles increase the hardness and fracture by a fatigue failure mechanism. Through this mechanism the fragment of the particles reduces the size because there's low agglomeration tendency. Due to the continued impact of the grinding balls the structure of the particles is constantly refined, but the particle size continues to be the same [8].

The milling process is affected by several variables such as the type of the mill, the material of milling media, the ball- to-powder ratio, the filling extent of the milling chamber, the milling atmosphere, the milling speed, the milling time [6].

The nature of the powders and chemical surroundings during the refinement of the microstructure can induce physical and chemical transformations [1,2,5].

The grain size of particles decreases during milling to some critical value, typically around 20 nm, depending on metal and processing conditions [9–12]. The kinetics of the refinement of grain size, showed that the reduction of grain size is due to the amount of powder effectively processed during each collision and by the hardness differences of the processed metals [13]. In many cases the particle size refinement is difficult due to the increase of aggregates. This effect was studied in solid phase and depends on the effect of aggregation and agglomeration that reduces effectiveness of milling.

3.1.2 Molecular level mixing

This method enables an optimal dispersion and avoid the thermal damage of graphene sheets during the synthesis of the composite. Generally, the large specific surface area of graphene makes difficult a homogeneous dispersion in matrix due to the tendency to form aggregates. Also, is necessary a process that not to destroy the sheet size of graphene [14]. The procedure consists in two steps. The first step consists in the functionalization of the graphene sheets making chemical bonds between graphene and the matrix. Next, the second step involve a procedure of sintering, like SPS, to obtain a bulk sample [15].

This strategies was applied successfully for graphene/Cu nanocomposites, also, carbon nanotube (CNT)/metal nanocomposites and for graphene/ceramic nanocomposites [14–17].

For instance, the Figure 4 is useful to represent a typical scheme of the synthesis through the MLM method. In this case, the graphite powder was chemical exfoliated, following the hummer method, obtaining graphene oxide [18]. Then graphene oxide was mixed with precursor salt of Cu to allow a good dispersion of the mixing constituents. The subsequently steps consist in the oxidation and reduction reactions to obtain the formation of graphene and at the same time the precipitation Cu powder. The last step consisting the sintering stage enable to obtain the composite bulk. With this procedure was obtained an optimal dispersion of graphene into Cu matrix and achieved improved mechanical properties [15].

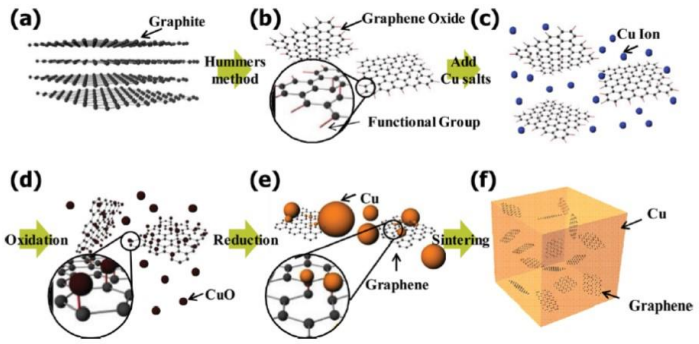

Fig. 4 Fabrication method to produce Cu-graphene nanocomposite. a and b) The procedure starts from the chemical exfoliation by Hummer method of graphite, c) Cu precursor was added to the dispersion of graphene oxide d) and c) oxidation and reduction steps to form graphene with consequently precipitation of Cu on the surface of graphene and f) sintering of composite powder to obtain the bulk [15].

Other examples of the MLM method found in literature involves the use of others precursors of Cu or with the use, directly, of a dispersion of graphene [19,20]. Moreover, others research works improved the dispersion of graphene into the matrix achieving good mechanical properties. Such as the addition of Ni nanoparticles to graphene flakes with the aim to avoid agglomeration and also to improve bonding strength between graphene and copper [21]. Or, in other cases, the use of surfactant in the solution, to improve the dispersion of graphene during the synthesis of Cu [14].

3.1.3 Spark Plasma Sintering Consolidation

Spark plasma sintering (SPS) is an alternative and innovative approach to conventional hot pressing. This methodology is a rapid sintering method with the advantages regarding the controlled grain growth and the enhancement of hot compaction up to full density.

SPS sintering is widely used to densify wide range of materials, from metals to ceramics, including different types of composites and coatings, as well as functionally graded materials [22–24].

SPS consolidate the powders through pulsed direct electric current passing across a powder sample compacted in a graphite mold [25]. A graphite mold is used to maintain the powders in an inert environment, and graphite plungers are used to press the powders. The consolidation process happens when the electrical current flows through the electrodes, graphite spacers, plungers, powders, and mold from positive electrode to negative one. The schematic equipment of SPS process is shown in Figure 5. The powders are inserted into a graphite mold and the sintering process is performed simultaneously by applying external pressure and electrical current [26].

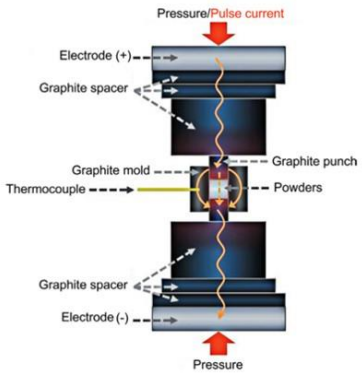

Fig. 5 A schematic view of the SPS apparatus [26].

There are different theories on what mechanisms are activated during the sintering of powders in SPS. According on experimental results or assumptions, one of these theories proposed is that the gases entrapped between particles can be ionized and transformed into plasma [27,28]. The mechanism of the SPS, anyway, remain unclear but three situations occur such as the activation by pulsed current, a resistance sintering (heating through electrical current passage) and the application of pressure [27,29–31]. It can also happen, sometimes, that the overheating on the particles surface leads to localized melting in the particle contacts [32].

Compared to the traditional sintering technologies, as shown in the Figure 6, the SPS method is more convenient and rapid due to the lower energy consumption, higher efficiency, extremely high heating rates up to 100°/min, short sintering times and the absence of sintering additives.

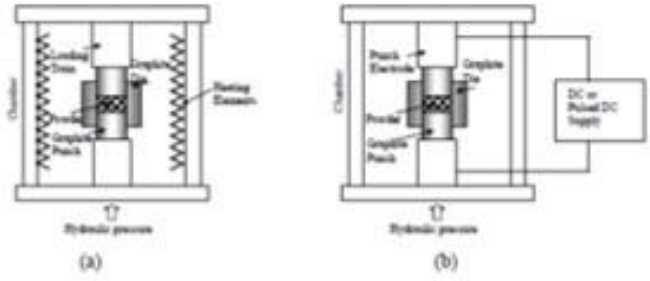

Fig. 6 Comparison between the apparatus schemes of hot pressing (HP) on the left and SPS on the right [33].

During the conventional HP, the heating of the sample is due to the radiation from the furnace, through external heating elements and, if applicable, the convection of inert gases. In this case there is a waste of heat due to the whole volume of space to heat before treating the powders [33].

On the other hand, the rapid sintering times of the SPS processes are characterized by the efficient use of the heat treatment and, also, allow to preserve the initial microstructure, to retain the fine grain size, the nanoscale, amorphous or crystal structure. Another impressive advantage is the applicability to sinter powder blends with various types of chemical bonding and electric conductivity [25].

Moreover numerous physical and mechanical properties could be enhanced by the SPS consolidation and for this reasons is regarded as an advanced technology [34–36].

The good electrical conductivity of the tooling materials of the SPS apparatus allow to use low voltages (typically <10 V) and to produce high currents (typically 1–10 kA) [37]. The densification takes place in very short time and this is possible due to the temperature rate that is up to 100C°/min saving also on energy costs [38].

In the SPS technology the small thermal gradients between the outside and the centre of the part ensure the elimination of residual stresses associated with thermal gradients. As it can be seen in Figure 7, another advantage associated to the use of SPS, the heating power is dissipated exactly at the locations in the microscopic scale, at the contact points of the powder particles, resulting in an optimal sintering behaviour with less grain growth and avoided powder decomposition [39].

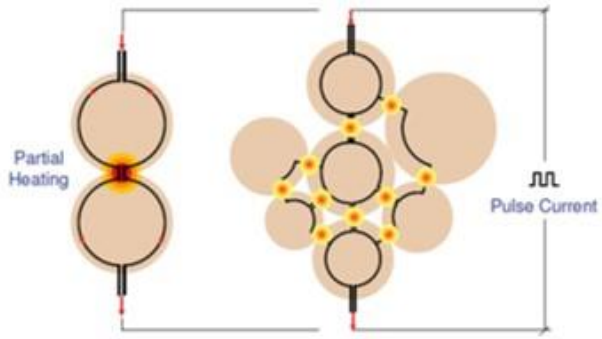

Fig. 7 Heating power distribution in the microscopic scale [39].

Bibliography

[1] C. Suryanarayana, Mechanical alloying and milling, Prog. Mater. Sci. 46 (2001) 1–184.

[2] M. Sopicka-Lizer, High-Energy Ball Milling, 2010. doi:10.1533/9781845699444.3.361.

[3] A. Care, P.L. Bergquist, A. Sunna, Solid-binding peptides: Smart tools for nanobiotechnology, Trends Biotechnol. 33 (2015) 259–268. doi:10.1016/j.tibtech.2015.02.005.

[4] P. Baláž, M. Achimovičová, M. Baláž, P. Billik, Z. Cherkezova-Zheleva, J.M. Criado, F. Delogu, E. Dutková, E. Gaffet, F.J. Gotor, R. Kumar, I. Mitov, T. Rojac, M. Senna, A. Streletskii, K. Wieczorek-Ciurowa, Hallmarks of mechanochemistry: from nanoparticles to technology, Chem. Soc. Rev. 42 (2013) 7571. doi:10.1039/c3cs35468g.

[5] Boldyrev VV, Mechanochemistry and mechanical activation of solids., Bull Acad Sci USSR Div Chem Sci. 39 (1990) 2029–2044.

[6] P. Baláz, Applied mechanochemistry. Mechanochemistry in Nanoscience and Mineral Engineering, Springer, Berlin Heidelberg;, 2008. doi:http://dx.doi.org/10.1007/978-3-540-74855-7_6. [68].

[7] F. Delogu, G. Gorrasi, A. Sorrentino, Fabrication of polymer nanocomposites via ball milling: Present status and future perspectives, Prog. Mater. Sci. 86 (2017) 75–126. doi:10.1016/j.pmatsci.2017.01.003.

[8] C. Suryanarayana, Mechanical Alloying and Milling Mechanical Engineering, Prog. Mater. Sci. 46 (2001) 1–184. doi:10.1016/S0079-6425(99)00010-9.

[9] B. Lasio, G. Pia, S. Garroni, R. Orrù, L. Takacs, F. Delogu, Non-monotonic variation of the grain size in Cu nanopowders subjected to ball milling, Mater. Lett. 212 (2018). doi:10.1016/j.matlet.2017.10.077.

[10] F. Delogu, G. Cocco, Crystallite size refinement in elemental species under mechanical processing conditions, Mater. Sci. Eng. A. 422 (2006) 198–204. doi:10.1016/j.msea.2006.02.032.

[11] F. Delogu, G. Cocco, The size refinement of Cu crystallites under mechanical processing conditions: A phenomenological modeling approach, J. Mater. Sci. 42 (2007) 4356–4363. doi:10.1007/s10853-006-0681-8.

[12] D.L. Zhang, Processing of advanced materials using high-energy mechanical milling, Prog. Mater. Sci. 49 (2004) 537–560. doi:10.1016/S0079-6425(03)00034-3.

[13] S. Garroni, S. Soru, S. Enzo, F. Delogu, Reduction of grain size in metals and metal mixtures processed by ball milling, Scr. Mater. 88 (2014) 9–12. doi:10.1016/j.scriptamat.2014.06.012.

[14] X. Gao, H. Yue, E. Guo, H. Zhang, X. Lin, L. Yao, B. Wang, Mechanical properties and thermal conductivity of graphene reinforced copper matrix composites, Powder Technol. 301 (2016) 601–607. doi:10.1016/j.powtec.2016.06.045.

[15] J. Hwang, T. Yoon, S.H. Jin, J. Lee, T.S. Kim, S.H. Hong, S. Jeon, Enhanced mechanical properties of graphene/copper nanocomposites using a molecular-level mixing process, Adv. Mater. 25 (2013) 6724–6729. doi:10.1002/adma.201302495.

[16] S. I. Cha, S.H.H. K. T. Kim , S. N. Arshad , C. B. Mo, Extraordinary Strengthening Effect of Carbon Nanotubes in Metal-Matrix Nanocomposites Processed by

Molecular-Level Mixing, Adv. Mater. 17 (2005) 1377.

[17] L. S. Walker, E.L.C. V. R. Marotto , M. A. Rafi ee , N. Koratkar, Toughening in Graphene Ceramic Composites, ACS Nano. 5 (2011) 3182.

[18] N.I. Zaaba, K.L. Foo, U. Hashim, S.J. Tan, W.W. Liu, C.H. Voon, Synthesis of Graphene Oxide using Modified Hummers Method: Solvent Influence, Procedia Eng. 184 (2017) 469–477. doi:10.1016/j.proeng.2017.04.118.

[19] D. Zhang, Z. Zhan, Strengthening effect of graphene derivatives in copper matrix composite, J. Alloys Compd. 654 (2016) 226–233.

[20] L. Wang, Z. Yang, Y. Cui, B. Wei, S. Xu, J. Sheng, M. Wang, Y. Zhu, W. Fei, Graphene-copper composite with micro-layered grains and ultrahigh strength, Sci. Rep. 7 (2017) 1–10. doi:10.1038/srep41896.

[21] M. Li, H. Che, X. Liu, S. Liang, H. Xie, Highly enhanced mechanical properties in Cu matrix composites reinforced with graphene decorated metallic nanoparticles, J. Mater. Sci. 49 (2014) 3725–3731. doi:10.1007/s10853-014-8082-x.

[22] R. Orrù, R. Licheri, A.M. Locci, A. Cincotti, G. Cao, Consolidation/synthesis of materials by electric current activated/assisted sintering, Mater. Sci. Eng. R Reports. 63 (2009) 127–287. doi:10.1016/j.mser.2008.09.003.

[23] R. Licheri, C. Musa, A.M. Locci, S. Montinaro, R. Orrù, G. Cao, L. Silvestroni, D. Sciti, N. Azzali, L. Mercatelli, E. Sani, Ultra-high temperature porous graded ceramics for solar energy applications, J. Eur. Ceram. Soc. (2018). doi:10.1016/j.jeurceramsoc.2018.01.023.

[24] H.S. Borkar T, Mohseni H, Hwang J, Scharf T, Tiley J, Spark plasma sintering (SPS) of carbon nanotube (CNT)/graphene nanoplatelet (GNP)- nickel nanocomposites: structure property analysis., Adv Compos Aerosp, Mar. L. Appl. (2015) 53–79.

[25] Ragulya AV, Fundamentals of spark plasma sintering., in: Elsevier (Ed.), Encycl. Mater. Sci. Technol. 2nd Ed., 2010: pp. 1–5.

[26] T.K. Nishikata K, Kimura A, Shiina T, Ota A, Tanase M, Fabrication and characterization of high-density MoO3 pellets., 2012 Powder Metall. World Congr. Exhib. (2012) 14–8.

[27] D. Tiwari, B. Basu, K. Biswas, Simulation of thermal and electric field evolution during spark plasma sintering, (2009). doi:10.1016/j.ceramint.2008.02.013.

[28] M. Tokita, Development of Large-Size Ceramic/Metal Bulk FGM Fabricated by

Spark Plasma Sintering, Mater. Sci. Forum. (1999). doi:10.4028/www.scientific.net/MSF.308-311.83.

[29] M.Z. Chen W, Anselmi-Tamburini U, Garay J, Groza J, Fundamental investigations on the spark plasma sintering/synthesis process: I. Effect of dc pulsing on reactivity., Mater Sci Eng, A. 394 (2005) 132–8.

[30] U. Anselmi-Tamburini, S. Gennari, J. Garay, Z. Munir, Fundamental investigations on the spark plasma sintering/synthesis processII. Modeling of current and temperature distributions, Mater. Sci. Eng. A. (2005). doi:10.1016/j.msea.2004.11.019.

[31] Lenel F., Resistance sintering under pressure., JOM. 7 (1955) 158–67.

[32] S.D. Pakdel A, Witecka A, Rydzek G, A comprehensive microstructural analysis of Al–WC micro-and nano-composites prepared by spark plasma sintering., Mater Des. 119 (2017) 225–34.

[33] M. Suárez, A. Fernández, J.L. Menéndez, R. Torrecillas, H.U. Kessel, J. Hennicke, R. Kirchner, T. Kessel, Challenges and Opportunities for Spark Plasma Sintering : A Key Technology for a New Generation of Materials, Sinter. Appl. (2013). doi:10.5772/53706.

[34] A. Azarniya, A. Azarniya, S. Sovizi, H.R.M. Hosseini, T. Varol, A. Kawasaki, S. Ramakrishna, Physicomechanical properties of spark plasma sintered carbon nanotube-reinforced metal matrix nanocomposites, Prog. Mater. Sci. 90 (2017) 276–324. doi:10.1016/j.pmatsci.2017.07.007.

[35] R.J. Kessel H.U., Hennicke J., Schmidt J., Weißgärber T., Kieback B., Herrmann M, “FAST” field assisted sintering technology- a new process for the production of metallic and ceramic sintering materials., (2008) p 1-37.

[36] A. Das, S.P. Harimkar, Effect of graphene nanoplate and silicon carbide nanoparticle reinforcement on mechanical and tribological properties of spark plasma sintered magnesium matrix composites, J. Mater. Sci. Technol. 30 (2014) 1059–1070. doi:10.1016/j.jmst.2014.08.002.

[37] M. Guillon, O., Gonzalez-Julian, J., Dargatz, B., Kessel, T., Schierning, G., Rathel, J., and Herrmann, Field-assisted sintering technology/spark plasma sintering: mechanisms, materials, and technology developments., Adv. Eng. Mater. 16 (2014) 830–848.

[38] T. Suarez, M., Fernandez, A., Menendez, J.L. Torrecillas, R., Kessel, H.U., Hennicke, J., Kirchner, R., and Kessel, Challenges and opportu- nities for spark

plasma sintering: a key technology for a new generation of materials., in: Sinter. Appl. Ertu , B. (Ed.). InTech. Ch. 13., 2010: p. 319–342.

[39] T. Kessel, H.U., Hennicke, J., KirchnerR, R. and Kessel, Rapid sintering of novel materials by FAST/SPS – further development to the point of an industrial production process with high cost efficiency., FCT Syst. GmbH, Rauenstein, Ger. (2009). http://fct-systeme.de/download/20100225123420/FCT-Sintered-Materials.pdf.

4. Experimental

4.1 Fabrication techniques

4.1.1 BM fabrication of Cu-MCs with nano graphite

Commercial high-purity Cu and graphite powders were subjected to BM in a SPEX 8000 (SPEX CertiPrep, USA) shaker mill, shown in Fig. 1.

Fig. 1 SPEX 8000 shaker mill with various types of reactors [1].

15 g of powders were inserted in a steel jar with 6 steel balls (2 of 8 g and 4 of 1g each), and milled, for 6, 12 and 24 hours with 15 min of rest time every hour. The powders (Cu and graphite) were weighed and loaded on a steel jar under Ar atmosphere, in glove box, to prevent the presence of oxygen during the milling time.

To find the best composition, various batches were prepared differing on the percentage in weight of graphite respect Cu. The compositions of 1, 3 and 5 wt.% of C to the total amount of powder were tested.

4.1.2 Preparation of Cu-MCs with nano graphite: two different way to add the reinforcement to the matrix

A batch of 5g of Cu mixed with 3 wt.% of C was prepared in a mortar and placed into the hardened steel reactor together with 2 stainless steel balls of 8g and 4 of 1g. The mixed powders were sealed under Ar atmosphere, the reactor was fixed to the mechanical arm of the SPEX miller, the powders were subjected to BM for 12h.

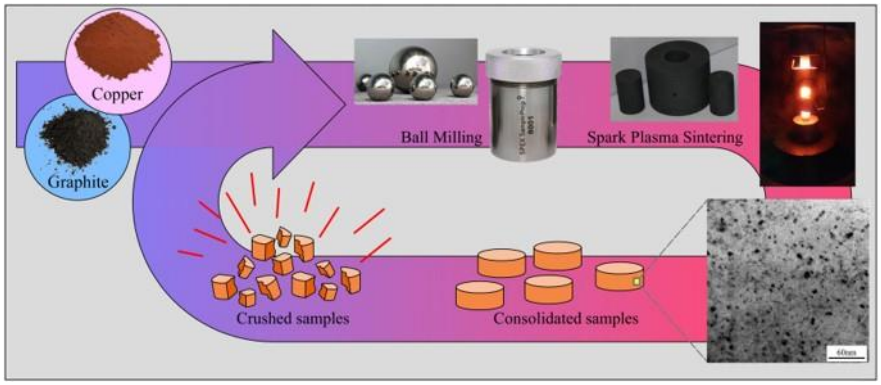

Fig. 2 Schematic stages of fabrication [2].

Then, the processed powders were consolidated by SPS. Finally, consolidated samples were crushed and the resulting granular material utilized for assembling new batches of 5 g.

The above-mentioned operation cycle was repeated up to 4 times to permit the progressive and simultaneous dispersion of graphite into the Cu grain, the refinement of the graphite to a nanometer size and the growth of the Cu to incorporate the dispersoid.

This procedure is shown schematically in Fig 2. Two different case studies were considered. In one case, at the beginning of a new cycle the reactor was simply re-filled with the granular material coming from crushed consolidated samples maintaining the amount of dispersed graphite constant at 3 wt%. In the other case, 3 wt% of graphite was added to the granular material at the beginning of every cycle. This resulted in a constant increase of the graphite content in the Cu-graphite MMC.

4.1.3 Synthesis of Cu-MCs with graphene by MLM

Cu chloride diidrate, ascorbic acid and graphene nanoplatelet dispersion were purchased from Sigma Aldrich. For the synthesis of Cu nanoparticles two solutions were prepared. The first solution was prepared with Cu chloride diidrate with a concentration of 0.18 M and the second consisted in a solution of ascorbic acid 1 M in water. [3]
In the case of Cu-graphene composite powder synthesis, a graphene dispersion was added to the solution of Cu chloride during stirring in the ratios with Cu of 0.5 or 1wt.%.
In the first step of the synthesis, the two solutions, before mixing, were adjusted at pH 7. Then the ascorbic acid solution was added to the Cu precursor solution (or Cu-graphene precursors solution) drop by drop and under stirring.
The reaction was conducted at 60°C and under stirring for four hours.
At the end of the reaction, the powders were collected by vacuum filtration and washed with water and ethanol. The filtrated powder was dried at 100°C overnight.

4.1.4 SPS consolidation

Consolidated samples of the processed powders were fabricated using a SPS 515 Sumitomo Coal Mining Co Ltd apparatus under a residual ambient pressure of 20 Pa. A calculated amount of powder depending on the theoretical mixture densities and bulk dimensions attended, was placed inside a cylindric graphite die, under Ar atmosphere, consisting of a dense graphite ring 30 mm high and with 10 and 23.4 mm of internal and external diameters respectively and symmetrically closed with plungers of 9.7 mm in diameter and 30 mm high, to obtain a bulk sample with diameter around 10 mm.
To facilitate the post-treatment sample release, the internal die surface was covered with a commercial graphite foil 0.13 mm thick.
Powders were densified increasing the temperature, at the rate of 100 °C min^{-1}, up to 950 °C (900 and 950 °C), and maintaining the sample at the desired temperature for 10 min. A low mechanical load of 32 MPa was applied during the consolidation of the powders.

4.2 Characterisation techniques

4.2.1 Density evaluation

Theoretical densities were calculated as a weighted average starting from the density of the pure components in the mixture multiplied for the percentage in volume of the Cu or graphite respectively.

The density of the samples was calculated by Archimedes' and geometrical methods.

Archimedes method is based in the weight of the sample when immersed in water. The density is calculated by the ratio between the dry weight and the difference of the humid and the immersed weight of the sample. To obtain the percentage density the result was divided with the theoretical value.

The geometrical method consists into the ratio between the weight and the volume of the consolidated sample. The ratio between the obtained values with the theoretical density for the mixture of pure copper and graphite give the percentage density.

4.2.2 X-ray diffraction (XRD)

Crystalline structure of powders and consolidated samples were characterized by X-ray diffraction (XRD) using a Rigaku Miniflex II X-ray diffractometer with a Cu K_α line (λ = 1.5405 Å) and, also, with a Philips PW 1830 X-rays diffractometer equipped with a Ni filtered Cu K_α radiation (λ=1.5405 Å).

Scattered intensity was collected over scattering angles from 30° to 80° with an angular step of 0.05° and a scan speed 0.2° min^{-1}.

The obtained XRD patterns were analysed by the Rietveld method using the Maud software comparing the experimental data with the tabulated crystalline phases in literature considering a good refinement with a value below 10 of the factor R_{wp} (weighted profile R-factor).

4.2.3 Raman Spectroscopy

The Cu-MCs were characterized by Raman spectroscopy to identify the type of C-based nanofiller obtained after the BM/SPS processing stages.

Micro-Raman scattering measurements were carried out on the samples in powder form in backscattering geometry using a 532 nm line by a wavelength, stabilized diode modules (Ondax Inc. Surelock LM series) and coupled with a Reflecting Bragg Grating (Optigrate – Braggrade 405) to narrow the laser line.

Measurements were performed with a triple spectrometer (Jobin–Yvonne Dilor) with a final spectral resolution of about 0.3 cm^{-1}. The beam was focalized by an Olympus microscope (100×, N.A. 0.95), the excitation beam power was kept below 200 μW in order to avoid heating effect (not observed for intensities 10 times larger and verified by anti-Stokes Raman analysis).

4.2.4 Scanning electron Microscopy (SEM)

The section of consolidate samples and, also, some powders were included in conductive resin and the surfaces were polished using grinding papers, from 400 to 4000 grits, to remove possible residues of the graphite foil and to better observation.

The microstructure of the powders and the consolidated samples were analysed by High-Resolution Scanning Electron Microscopy (HRSEM, mod. S4000, Hitachi, Tokyo, Japan) and, also, SEM–EDS instrument Zeiss Evo LS15 environmental scanning electron microscope (Carl Zeiss SMT AG, Germany), LaB6 cathode, EHD 5 kV, WD 13.5 mm.

4.2.5 Transmission Electron Microscopy (TEM)

The microstructure of consolidated samples was studied by transmission electron microscopy (TEM) using a Philips CM-20, equipped with liquid-N_2 double tilt specimen holder. TEM discs were prepared by conventional mechanical grinding and polishing, followed by double side dimpling, and finally, by ion-milling, using a Gatan© PIPS facility, operated at an ion beam energy of 4 kV with incident angles of 8, 6, and 4°,

respectively for the first half, the second quarter, and the final quarter of the preparation stage.

4.2.6 Nano Indentation

A Hysitron Inc. triboscope nanoindenter Ubi-1 was used to determine Young's modulus and hardness of consolidated samples. Uniaxial compression was performed using a 3-sided pyramidal Berkovich tip with edge aperture angle of 65.35° and radius of curvature of 150 nm. A pyramidal load function was used. Accordingly, the sample was subjected to incremental load for 10 s, held for 20 s at the maximum load of 8000 mN, and finally unloaded within 10 s. Each nanoindentation test involved 100 individual measurements from a matrix of 10×10 points, 150 μm spaced from each other and spanning a surface area of 1.5 mm^2. Experiments were performed on consolidated samples with suitably polished surfaces.

For Strain Rate Sensitivity (SRS) studies the nanoindentation measurements were analysed using the Oliver and Pharr method [4–6]. Hardness, H, and reduced Young's modulus, Er, were obtained through a complete cycle of load-unloading procedure.

The unloading curve was fitted with the relationship $P= B (h-h_f)^k$, where P is the tip load, h the displacement, h_f is the displacement after unloading, B and k are the fitting parameters.

The penetration contact depth, hc, can be estimated by $hc= h_{max}-\eta \left(\frac{P_{max}}{S}\right)$, where h_{max} is the maximum indenter penetration depth in correspondence of maximum applied load, P_{max}, η is a constant relative to the tip and S is the material stiffness. For a Berkovich tip the constant is η=0.75.

The calibration, necessary before the SRS analysis, was carried out on fused quartz (Er ¼ 72 GPa) according to the round robin experiment protocol [7]. A Trapezoidal load functions, consisting of equal load and unload rates to and from the peak load P_{max}, and different dwelling times, td, were used. In particular, the load, P, vs. penetration depth, hc, measurements were performed at different strain rate, ε, by changing the loading rate from 0.0025 to 0.5 s^{-1}, at a maximum load P_{max} = 10 mN. The indentation strain rate was computed by $\varepsilon = \frac{P}{P'}$, where P' is the loading rate, and P the maximum load.

In order to study the creep response, the four different samples were held at the maximum load. Different dwelling times, td, 5, 15, 30, 60, 90, 120, 180, 240, and 300 s, are respectively considered. The nanoindentation matrix of measurements involved a typical sample area of about 2 mm^2.

Bibliography

[1] SPEX mixer mill 8000, (n.d.). https://www.fishersci.co.uk/shop/products/shaker-mixer-mill/12548696.

[2] B. Lasio, F. Torre, R. Orrù, G. Cao, M. Cabibbo, F. Delogu, Fabrication of Cu-graphite metal matrix composites by ball milling and spark plasma sintering, Mater. Lett. 230 (2018) 199–202. doi:10.1016/j.matlet.2018.07.120.

[3] Q.M. Liu, T. Yasunami, K. Kuruda, M. Okido, Preparation of Cu nanoparticles with ascorbic acid by aqueous solution reduction method, Trans. Nonferrous Met. Soc. China (English Ed. 22 (2012) 2198–2203. doi:10.1016/S1003-6326(11)61449-0.

5. Results and discussion

The research activity has undergone several phases. In the first phase the optimization of the operative conditions for the fabrication of the Cu-MCs reinforced with graphite has been carried out. Next, in the second phase, a methodology to achieve an atomic forced mixing has been defined and consisted in a combination of consecutive BM and SPS stages. In the third phase, through the nanoindentation test has been analysed a selected series of Cu-C samples to determine the strain rate sensitivity (SRS) of the material. Finally, in the last phase of the research, for comparison, another method of dispersion, the molecular level mixing, has been tested to fabricate Cu-MCs reinforced with graphene.

5.1 Fabrication of Cu-MCs reinforced with nano graphite by a top-down approach

5.1.1 Optimization of the operative conditions of BM and SPS

The powders of Cu and composite powders with Cu and 1, 3 and 5 wt.% of graphite were milled for different time such as 0.5, 6 and 24 hours. The composite powders were prepared in a mortar mixing Cu with graphite in the various compositions and then placed into a steel jar for the processing through BM. All the working operations were carried out under Ar atmosphere, in a glove box, to avoid the oxidation of the powder.
The processed powders were, then, characterised by XRD and SEM to determine the crystalline phases and the microstructure obtained.
The comparison between the patterns of the Cu powder samples before and after 24 hours of milling is shown in Figure 1. The reflections of the two samples are similar, they exhibit the typical peaks relative to a Cu cubic phase, without any presence of Cu oxides. The two patterns show different intensity of the peaks, the sample relative to the 24 h of BM is lower and also presents larger peaks due to the reduction of the crystallite size.

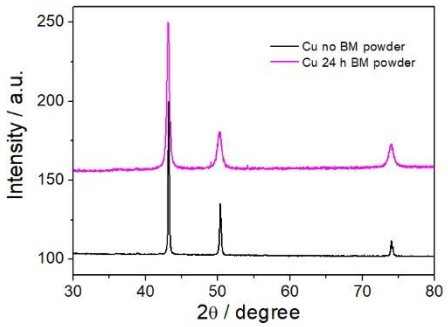

Fig. 1 XRD diffraction patterns of Cu powders before and after 24 hours of BM.

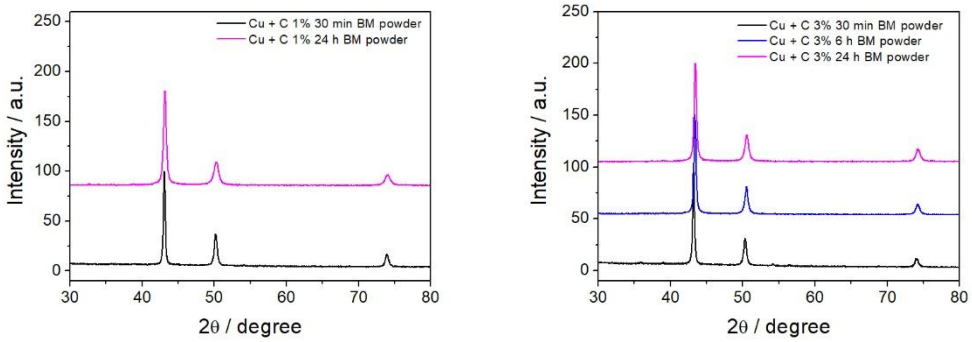

Fig. 2 XRD diffraction pattern of the composite powders a) Cu mixed with 1 % of graphite after 30 min and 24 hours of BM and b) Cu mixed with 3 % of graphite after 30 min, 6 and 24 hours of BM.

Then, the composite powders were prepared, mixing Cu with 1 or 3 wt.% of graphite, then milled by BM for various time such as 0.5, 6 and 24 hours. Also, in this case, the operative procedures were conducted under Ar.

The XRD patterns of the composite powders relative to Cu with 1 and 3 % of graphite are shown in Figure 2. The patterns of the composites exhibit analogous peaks relative to a Cu cubic phase for all the times of milling with no difference respect the Cu powder reflections.

The results of the Rietveld refinement analysis are presented in Table 1. All the processed powders patterns presented an increase in cell parameter and a decrease in crystallite size after 24 hours of milling.

In particular, in the case of Cu-C 3 wt.% after 24 h of BM the cell parameter increases up to 3.619, this effect is probably due to the incorporation of graphite into the grain. While

slight variations are noted on the crystallite size in the case of 1 and 3 % of C and after 24 h respect the Cu.

The processed powders were, also, characterised by SEM microscopy to evaluate the microstructure of the particles. In Figures 3 and 4 are reported the SEM micrographs of composite powders. The dimension of the particles of composite powder Cu-C 1 wt.% of C after 24 hours of BM, is about 42 μm. While considering the case of Cu-C 3 wt.% the dimensions of the powders are minor around to 28 μm, the addition of more graphite into the composite allows a reduction in the size of the particles during the milling.

Tab. 1 XRD parameters, cell parameter, crystallite size and microstrain, obtained by the Rietveld refinement of the XRD patterns of Cu and the composite (Cu-C 1wt.% and Cu-C 3wt.%) powders.

Samples Powders	**BM**	**Cell parameter (Å)**	**Crystallite Size (nm)**	**Microstrain**	**Rw %**
Cu	0h	3.615	209.5	$4.63 * 10^{-4}$	10.2
	24h	3.616	39.0	0.002	8.5
Cu-C 1 wt.%	0.5h	3.614	85.3	0.001	8.2
	24h	3.615	34.0	0.002	6.8
Cu-C 3 wt.%	0.5h	3.616	82.3	0.001	10.7
	6h	3.619	44.6	0.001	6.7
	24h	3.619	40.9	0.002	6.5

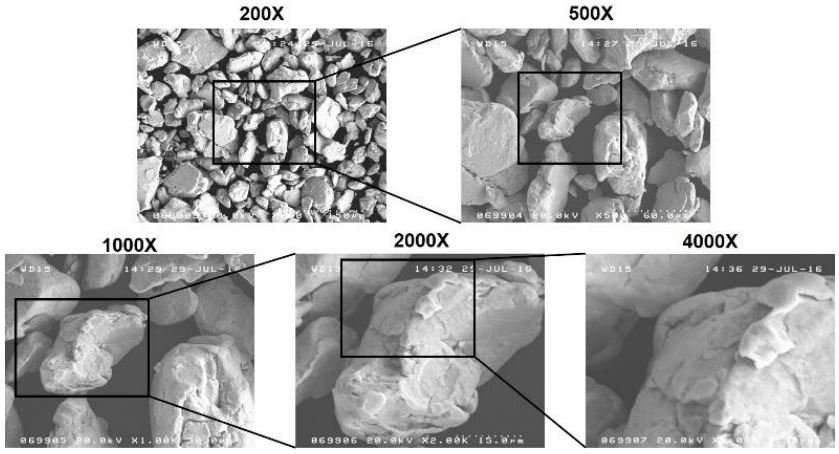

Fig. 3 SEM micrography of Cu-C 1 wt.% composite powder after 24h BM at various magnifications.

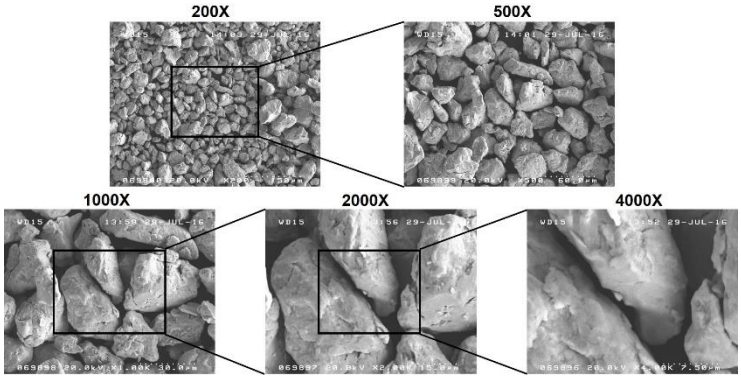

Fig. 4 SEM micrography of Cu-C 3 wt.% composite powder after 24 hours of BM at different magnifications.

The BSE-SEM micrographs at high magnification of the composite powders are shown in Figures 5 and 6. In this visualization the difference between the phases is a little bit highlighted. The graphite, after 24 h of BM, seems to be placed as a coating on the surface of the particles of the composite.

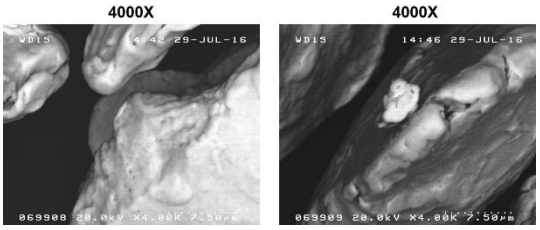

Fig. 5 BSE-SEM micrographs of the composite powders based on Cu with C 1% 24h BM at high magnification.

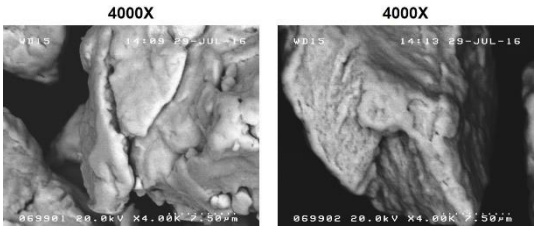

Fig. 6 BSE-SEM micrographs of the composite powders based on Cu-C 3% 24h BM at high magnification.

Subsequently, the processed powders were consolidated through SPS at 900 and 950°C to find the optimal temperature of sintering. An amount of powder based on the theoretical density of the mixture powder and the volume of sample attended was placed on the SPS mold and was subjected to the sintering process.

The calculated densities of the Cu sintered sample are shown in Table 2.
As it can be seen in the table 2, all the samples reach almost the full density, ranging from 87 to 100 %. But, it is to underline that, the sintering process at 950 °C is near to the melting point of Cu that is at 1085°C. In fact, during several densification treatments of the powder the process failed because the sample has melted. Probably the oscillation of the temperature heats more than the temperature of 950°C reaching the melting point.

Tab. 2 Density values of Cu bulk samples milled at different time (0, 6 and 24 hours) and consolidated through SPS at 900 and 950°C for 10 minutes.

Samples	**BM**	**(ϱA)** **ϱA%**	**(ϱG)** **ϱG%**
		SPS 950°C	
Cu **ϱ= 8.96** **g/cm^3**	**0 h**	(8.7) 97%	(9.3) 104%
	6h	(7.8) 87%	(7.8) 87%
	24h	(7.7) 86%	(7.8) 87%
		SPS 900°C	
	0h	(8.7) 97%	(9.2) 103%
	6h	(8.2) 91%	(8.2) 91%
	24h	(7.6) 85%	(8.0) 89%

In Figure 7, are reported the XRD patterns of the Cu sintered samples treated at 900 and 950°C for 10 minutes. The reflections of all the samples, as it can be noticed in the figure, exhibit the pattern of the Cu cubic phase with any presence of oxides. The intensity and the width of the peaks are different considering the two temperatures of treatment. The peaks, in the case of 950°C, are higher and less wide due probably to larger dimensions of the crystallites.

The patterns of the Cu consolidated samples were, also, analysed by the Rietveld method to determine the XRD parameters. The cell parameter, crystallite size and microstrain of Cu sintered samples at 900 and 950°C are shown in Table 3.

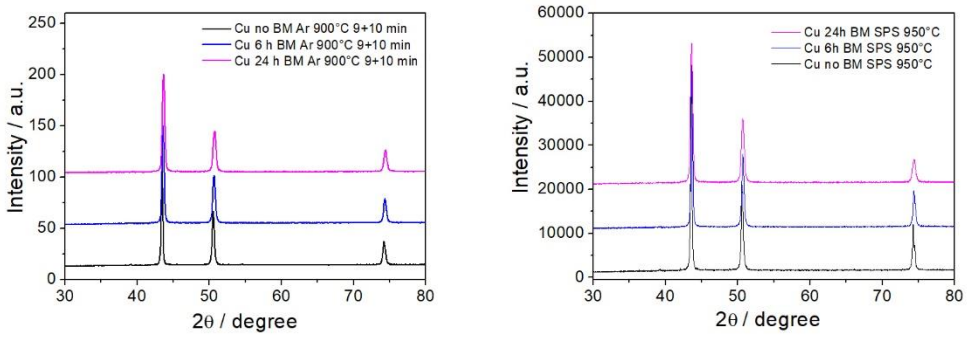

Fig. 7 XRD diffraction pattern of the SPS sintered samples of Cu powders milled for different time (0, 6 and 24 hours) and consolidated through SPS at 900 (at left) and 950°C (at right) for 10 minutes.

In the table, it can be noticed that the sintering process influence slightly the cell parameter and more the crystallite size, especially in the case of 950°C. Comparing with the Cu processed powders milled 24 h, after the sintering treatment the crystallite size of Cu bulk samples increases up to 80.3 (at 950°C) and 69.8 (at 900°C) nm with respect to 39 nm.

Tab. 3 XRD parameters, cell parameter, crystallite size and microstrain, obtained by the Rietveld refinement of the XRD patterns of the composite powders of copper no BM and BM at 6 and 24 h and sintered at 900°C and 950°C.

Samples	**BM**	**Cell parameter (Å)**	**Crystallite Size (nm)**	**Microstrain**	**Rw %**
		SPS **950°C**			
Cu	**0h**	3.624	117	$4.98*10^{-4}$	9.9
	6h	3.624	99.4	$8.93*10^{-4}$	9.0
	24h	3.623	80.3	0.002	7.3
		SPS **900°C**			
	0 h	3.623	79.7	0.001	8.2
	6h	3.623	76.4	0.001	8.1
	24h	3.624	69.8	0.002	7.3

The composite powders of Cu-C 1 wt.% were, also, consolidated by SPS at 900 and 950°C for 10 min and characterised.

In Tab 4 are reported the calculated densities of the Cu-C 1wt.% composites sintered at 900 and 950°C. Comparing these densities with the result of the consolidated Cu, it can be noticed that the addition of 1 wt. % of C slightly increases the densities, in particular in the cases of 6h and 24 h milled powders and treated at 900°C. The other values are about similar to the densities of the Cu bulks.

Tab. 4. Density values of the composite samples Cu-C 1 wt.% milled at 0.5, 6 and 24 h and sintered at 900 and 950°C.

Samples	**BM**	**(ϱA) ϱA%**	**(ϱG) ϱG%**
		SPS 950°C	
Cu-C 1wt.% ϱ_{mix} **= 8.69 g/cm^3**	**0.5h**	(8.60) 99.1%	(8.7) 100.3%
	6h	(8.53) 98.2%	(9.18) 106%
	24h	(7.46) 85.8%	(7.66) 88.2%
		SPS 900°C	
	0.5 h	(8.25) 94.9%	(8.86) 102%
	6h	(7.89) 90.8%	(8.30) 95. 6%
	24h	(7.62) 87.7%	(8.36) 96.3%

The reflections of the sintered samples Cu-C 1 wt.% consolidated at 900 and 950°C are shown in Figure 8. Also, in this case, the addition of graphite and the thermal treatments of 900 and 950°C doesn't affect the crystalline phase exhibited, showing only the Cu cubic phase. There is to underline that, also in this case, the treatment at 950°C is susceptible to oscillation increasing up to 1085°C and many times during the sintering the powders melted.

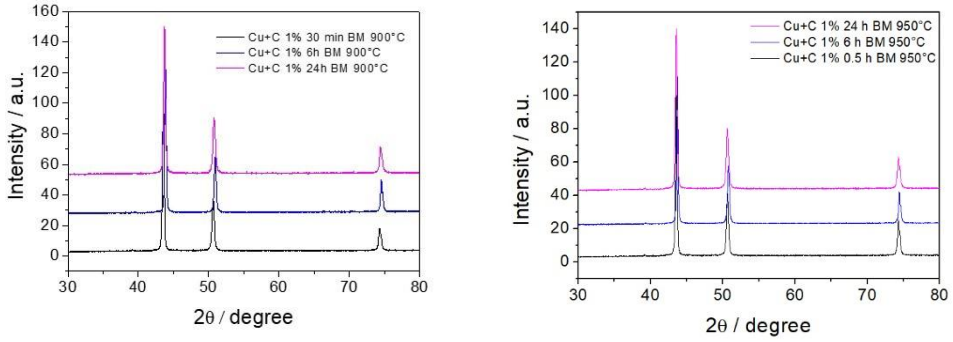

Fig. 8 XRD diffraction pattern of the sintered samples of composite powders based on Cu-C 1 wt.% milled for different time (0.5, 6 and 24 hours) and treated in SPS at 900 (at left) and 950°C (at right) for 10 minutes.

The Rietveld refinements results are shown in Table 5. The cell parameters show an increase up to 3.625 in particular in the cases treated at 900°C of Cu-C 1 wt.% 6 and 24 hours milled. This increase should be due to the incorporation of graphite into the grain of Cu.

The crystallite size shows an increase respect the Cu bulk sample, in particular for the Cu-C 1wt.% 6 hours milled and the sintered at 950°C that reaches about 122 nm.

Tab. 5 XRD parameters, cell parameter, crystallite size and microstrain obtained by the Rietveld refinement of the XRD reflections of the composite samples Cu-C 1 wt.% milled at 0.5, 6 and 24 h and the sintered at 900 and 950°C.

Samples	**BM**	**Cell parameter (Å)**	**Crystallite Size (nm)**	**Microstrain**	**Rw %**
		SPS 950°C			
Cu-C 1wt.% ϱ_{mix} **= 8.69 g/cm^3**	**0.5h**	3.622	105.1	$8.1*10^{-4}$	7.2
	6h	3.623	122	$4.7*10^{-4}$	7.9
	24h	3.623	89.7	0.001	7.5
		SPS 900°C			
	0.5 h	3.621	92.6	0.001	6.4
	6h	3.625	105.6	$6.7*10^{-4}$	7.1
	24h	3.625	86.7	0.001	7.5

Furthermore, the processed powders of Cu-C 3 wt.% were consolidated, selecting only the more stable treatment at 900°C for 10 minutes.

The densities of the consolidate samples of Cu-C 3 wt.% are shown in Table 6. This composition and thermal treatment seem to achieve a better condition of densification respect the other composition. As it can be noted in the table, in this case, the geometrical density reaches values from 95 to 100%.

In Figure 9 the patterns of Cu-C 3 wt.% consolidated at 900°C are shown. The reflections, also in this case, show the typical pattern of Cu cubic phase with no presence of oxides. Between the XRD patters there's a difference regarding the intensity and width of the peaks.

The XRD parameters calculated by the Rietveld refinement are shown in Table 7. Here, it can be noticed that an increase of cell parameter due to the BM processing and probably to the incorporation of graphite. Considering the crystallite size values, the increase in the case of 6 h of BM reaches up to 96 nm and for 24 h up to 77 nm.

Another composition, the powder constituted of Cu-C 5 wt.%, was also tested.

In Table 8 are shown the values of the densities relative of these samples. The sintering of the processed powders at 900°C enable to obtain densities between 96 to 108 % almost similar to the previous composition Cu-C 3 wt.%.

Tab. 6 Density values of Cu-C 3 wt.% processed by BM for different time (0.5, 6 and 24 h) and sintered at 900°C for 10 min.

Samples	**BM**	**(ϱA)** **ϱA %**	**(ϱG)** **ϱG %**
		SPS 900°C	
Cu-C 3 wt.% **ϱ_{mix}= 8.21** **g/cm^3**	**0.5 h**	(8.18) 99.7%	(8.6) 105%
	6 h	(7.71) 93.9%	(8.54) 104%
	24 h	(7.68) 93.6%	(7.81) 95.2%

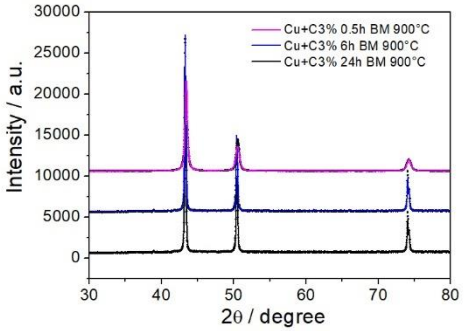

Fig. 9 XRD diffraction pattern of the SPS sintered samples of Cu-C 3wt.% of BM for 0.5, 6 and 24 hours and treated in SPS at 900°C for 10 minutes.

Tab. 7 XRD parameters, cell parameter, crystallite size and microstrain obtained by the Rietveld refinement of the composite powders and Cu-C 3 wt.% processed by BM for different time (0.5, 6 and 24 h) and sintered at 900°C for 10 min.

Samples	**BM**	**Cell parameter (Å)**	**Crystallite Size (nm)**	**Microstrain**	**Rw %**
Cu-C 3 wt.% Powders	**0.5h**	3.6163	82.3	0.001	10.7
	6h	3.6193	44.6	0.001	6.7
	24h	3.6196	40.9	0.002	6.5
Cu-C 3 wt.%		**SPS 900°C**			
		Cell parameter (Å)	**Crystallite Size (nm)**	**Microstrain**	**Rw %**
ϱ_{mix}= 8.21 g/cm^3	**0.5h**	3.6164	145.7	$1.212*10^{-4}$	6.0
	6h	3.6186	96.62	0.001	8.1
	24h	3.6219	77.5	0.001	5.9

Tab. 8 Density values of the composite materials based on Cu-C 5 wt.% milled at different time (0.5, 6 and 24 hours) and consolidated at 900°C for 10 minutes.

Samples	**BM**	**(ϱA) ϱA %**	**(ϱG) ϱG %**
		SPS 900°C	
Cu + 5% C ϱ_{mix} **= 7.78 g/cm^3**	**0.5 h**	(7.5) 96.4%	(8.4) 108%
	6h	(7.13) 91.6%	(7.04) 91%
	24h	(7.03) 90.3%	(7.5) 96.5%

The XRD patterns of Cu-C 5 wt.% are shown in Figure 10. The reflections exhibit, like the previous cases, the formation of Cu cubic phase without the presence of oxides and other species.

In Table 9 are presented the Rietveld refinements result of the Cu-C 5wt.% composites samples. Considering the cell parameter, it can be noticed that every milling and thermal treatments reach almost the same results. Probably this excess of composition in graphite is not able to enter in the cell of Cu. While the grain size increase in the case of 6 hours and decrease for 24 hours of milling.

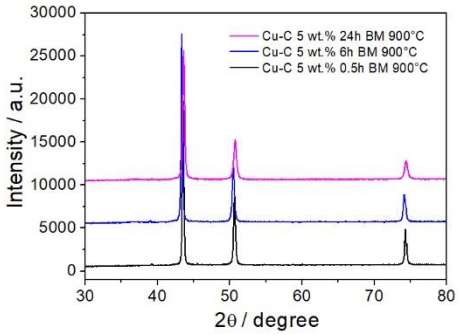

Fig. 10 XRD diffraction pattern of the SPS sintered samples of Cu-C 5 wt.% of BM for 0.5, 6 and 24 hours and treated in SPS at 900°C for 10 minutes.

Tab. 9 XRD parameters, cell parameter, crystallite size and microstrain, obtained by the Rietveld refinement of the XRD patterns of the composite samples Cu-C 5 wt.% ball milled different time (0.5, 6 and 24 h) and sintered at 900°C.

Samples	**BM**	**Cell parameter (Å)**	**Crystallite Size (nm)**	**Microstrain**	**Rw %**
		SPS 900°C			
Cu + 5 % C	**0.5 h**	3.62	113	$1.18*10^{-4}$	6.4
	6h	3.62	109.9	$7.98*10^{-4}$	6.6
ϱ_{mix} **= 7.78 g/cm^3**	**24h**	3.62	59.8	0.001	5.6

The sections of the consolidated samples at 900 °C of Cu, Cu-C 1wt.% and Cu-C 3 wt.% was analysed by SEM microscopy.

In Figure 11 is shown the section of Cu no BM sample at various magnifications. This sample exhibits a homogeneous surface without presence of holes or fractures.

The SEM micrographs of Cu bulk sample after 24h of BM and consolidated at 900°C are shown in Figure 12. In this case, it can be noticed the effect of 24 hours of milling in Cu bulk. The surface of the sample appears less homogeneous and with the presence of small defects.

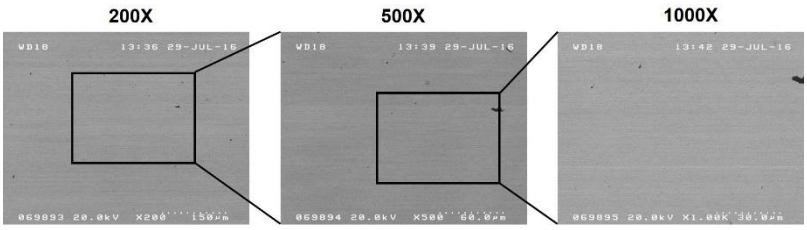

Fig. 11 BSE-SEM images of the sample Cu no BM sintered in SPS at 900°C.

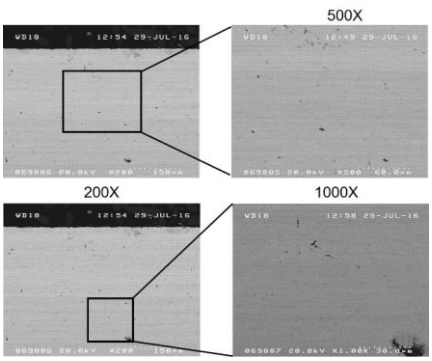

Fig. 12 BSE-SEM images of the sample Cu 24h BM sintered in SPS at 900°C for 10 min.

In Figure 13, is reported the SEM micrography of the section of the Cu-C 3 wt.% sample treated 30 minutes by BM and sintered at 900°C. In the figure, the presence of graphite can be identified by the black parts distributed into the matrix. This sample was processed for short time of milling but it is a sufficient time to achieve almost homogeneous distribution of graphite and a formation of a composite structure with embedded dispersoids.

The Cu-C 3wt% section milled for 24 hours and treated at 900°C is shown in Figure 14. The increased time of milling, for this composition, achieves to obtain a lamellar structure composite where the graphite is incorporated into the matrix.

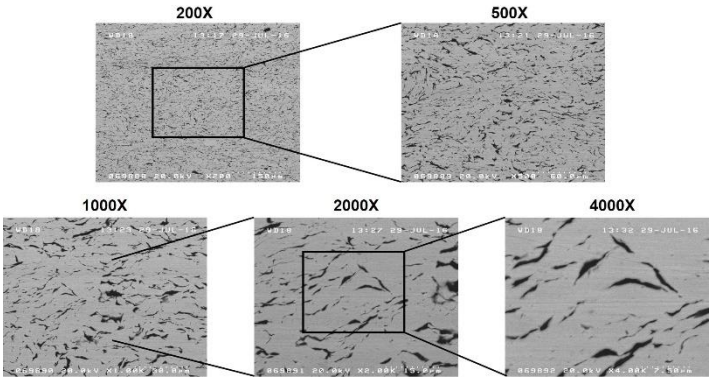

Fig. 13 BSE-SEM images of the sample Cu-C 3 wt.% 30 min BM sintered in SPS at 900°C.

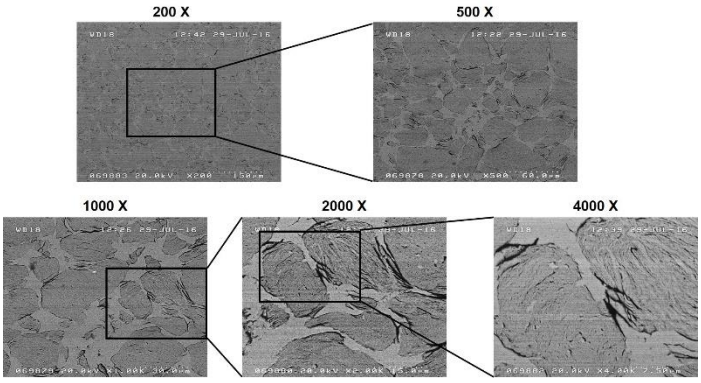

Fig. 14 BSE-SEM images of the sample Cu-C 3 wt.% 24h BM sintered in SPS at 900°C.

The samples of Cu-C 3wt.% milled for 0.5 and for 24 hours and consolidated at 900°C were selected to determine the mechanical properties by nanoindentation.

In Table 10 the results of nanoindentation tests are reported. In the table, it can be noticed, that the increase of the milling time affects positively the hardness and the elastic

modulus. In fact, the sample milled for 24 hours increases the hardness up to 275 while the 0.5 hours milled reaches the value of 137.

Same behaviour can be seen in the case of elastic modulus, where the sample milled for 24 h reaches the value of 62 GPa while the other attains 38 GPa.

In comparison with other results found in literature, it can be noted that, in this case greater values of hardness and elastic modulus has been achieved. In particular, considering the work of Li et al., where graphene has been dissolved by ultrasonication into Cu powder and subsequently consolidated to obtain a bulk sample. The mechanical properties of the composite, achieved through this dispersion methodology, attain minor values of hardness and elastic modulus, 74.2 and 0.185 GPa respectively, respect to the results achieved here [1].

Tab. 10 Mechanical properties of the Cu-C 3 wt.% samples obtained by nanoindentation test.

Samples	**BM**	**HV**	**E GPa**
		SPS 900 °C	
Cu-C 3 wt.%	**0.5 h**	137	38
	24 h	275	62

These exploratory studies allowed to define a promising composition from the point of view of density and crystallographic data. The composition Cu-C 3 wt.% was selected for the following experiments. SEM microstructural observations also allowed us to define grinding and sintering parameters. The intermediate milling time of 12 hours it has been chosen and selected 900°C as SPS sintering temperature.

Through the observation of the SEM micrographs has been possible to notice that, the composites obtained so far, do not show a level of microscopic mixing.

Instead, the results of the nanoindentation tests has shown promising values in hardness and elastic modulus.

Based on these results, the composition Cu-C 3wt.% was selected to continue with the subsequent experiments.

5.1.2 Preparation of Cu-MCs with nano graphite: two different way to add the reinforcement into the matrix

The cyclic exposure of Cu-graphite powder mixtures and granules to BM and SPS conditions affects the Cu and graphite microstructures. Microstructural evolution is sensitive to the total amount of graphite involved in experiments. For clarity, the case studies involving no addition (CS1) and constant addition (CS2) of graphite are discussed separately.

The average of the densities, calculated by geometric method, of the samples CS1 and CS2 are shown in Table 11. It can be noticed that, for the CS2 samples, where was added graphite in every stages of treatment, a decrease of density ranging from 82 to 95 %. In this case an excess of dispersoid does not favour the process of densification. In contrary, in the case of CS1, where graphite was added only at the first stage, there's an increase of density from 95 to 99%. In that case, the right amount of dispersoid and the stages of BM/SPS treatment allow to obtain a fully dense bulk.

Tab. 11 Density values of the composite materials Cu-C 3 wt.% CS1 and CS2 subjected to BM/SPS stages.

Sample	**BM/SPS step**	**ϱ_{mix}**	**ϱG**	**ϱG %**
	SPS 900°C			
Cu-C 3 wt.% CS2	1	8.21	7.8	95
	2	7.53	6.8	90
	3	7.03	5.8	83
	4	6.60	5.4	82
Cu-C 3 wt.% CS1	1	8.21	7.8	95
	2	8.21	7.8	95
	3	8.21	7.9	97
	4	8.21	8.17	99

XRD patterns of CS2 powders and consolidated samples at every processing cycle are shown in Figs. 15a and 15b respectively. The powder XRD reflections, after BM, exhibit similar broadening. This means that Cu is nanostructured. It can be noticed, in figure15,

the presence of a slight shift of XRD peaks towards small scattering angles which suggests that the Cu unit cell parameter has increased, probably due to the incorporation of graphite into the matrix. The peaks of graphite are not visible because the amount is lower than the detectable limit. XRD patterns of consolidated samples exhibit sharper peaks, which can be ascribed to the formation of larger Cu grains due to the SPS treatment.

The Rietveld analysis of XRD patterns results in the grain size estimates are shown in Fig. 15c. The grain size of powders, instead, remains constant around the value of 30 nm, while, for consolidated samples it increases up to 120 nm. In this case, the addition of graphite in every stages of processing favour the grain growth of Cu, reaching the dimension of 120 nm.

A different behaviour emerges from the XRD patterns collected from CS1 powders and consolidated samples, which are shown in Figs. 16a and 16b respectively. The XRD patterns of CS2 powders almost overlap with those of CS1 powders, which suggests that CS1 and CS2 powders have similar microstructure. Conversely, the XRD peaks of CS2 consolidated samples are narrower than those of CS1 powders.

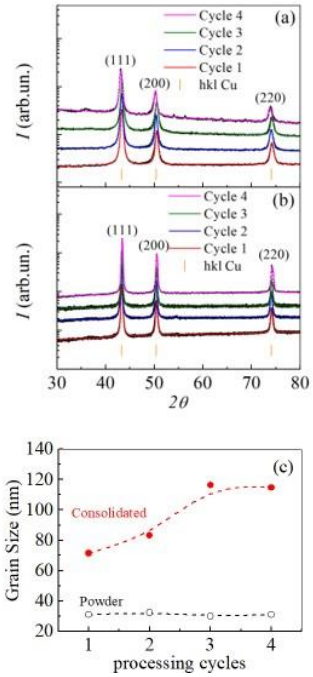

Fig. 15 XRD patterns of CS2 powders and consolidated samples measured at the end of each stage of treatment: a) XRD patterns of initial Cu-graphite powder mixtures, b) XRD patterns of consolidated samples, c) average grain size of CS2 powders (black graph) and consolidated samples (red graph).

The Rietveld analysis confirms such considerations. As shown in Fig. 16c, powders have grain size around 30 nm, whereas consolidation makes it increase to about 70 nm. In both cases, grain size of powders is almost insensitive to the number of cycles.
Overall, experimental results indicate that SPS induces significant grain growth. Starting from about 30 nm for powders, grain size reaches 70 and 120 nm for CS1 and CS2 consolidated samples respectively. In principle, the observed differences in grain growth can be ascribed to the different graphite content in CS1 and CS2 consolidated samples.

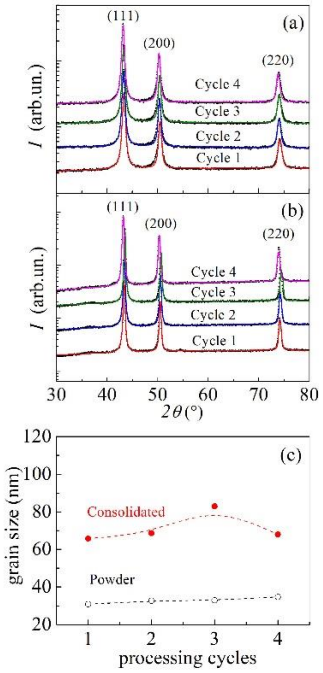

Fig. 16 XRD patterns of CS1 powders and consolidated samples measured at the end of each stage of treatment: a) XRD patterns of initial Cu-graphite powder mixtures, b) XRD patterns of consolidated samples, c) average grain size of CS1 powders (black graph) and consolidated samples (red graph) [7].

Raman spectroscopy of graphite powder and consolidate samples CS1 and CS2 is shown in Figure 17. It can be noticed that graphite, after the BM/SPS stages, changes aspect becoming a graphene like structure. The consecutive stages of BM and SPS exfoliate and refine the structure of micrometrical graphite to a graphene-like dispersoid. As seen in the figure, the graphite spectra exhibit an intense G band associated to a graphitic material, while the processed bulk samples show, also, the D peaks relative to a graphene-like structure. This type of structure can be ascribed to a graphite nanocrystalline material

as it can be found in literature [2]. The ratio between the intensity of the two peaks D and G is around the value of 1, depends on the number of the defects of the carbons structures [3,4]. As it can be verified in literature such type of structure is ascribed to a multilayer nano graphite [5,6].

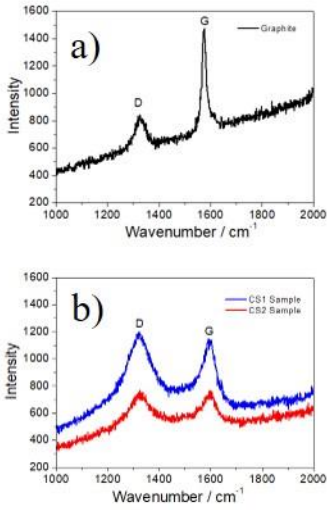

Fig. 17 Raman spectroscopy of a) graphite powder and b) the Cu-C 3 wt.% CS1 (blue graph) e CS2 (red graph) bulk samples after the fourth step of treatment.

Graphite content also plays a clear role in the definition of mechanical properties for consolidated samples. Hardness and elastic modulus measured by nanoindentation of CS1 and CS2 consolidated samples are shown, respectively, in Figs. 18a and 18b, as a function of the number of cycles. For convenience, data are plotted on a relative scale, hardness and elastic modulus values being normalized to the corresponding estimates obtained for pure Cu samples subjected to the same processing conditions. As evident from Fig. 18b, the relative hardness, Hr, of CS2 consolidated samples decrease smoothly as the number of cycles increases. Opposite trend is shown by CS1 consolidated samples where the Hr increase up to 25 % respect to Cu. Data relative to the elastic modulus, Er, for CS1 and CS2 in Fig. 18a and b indicate a similar behaviour like Hr. It decreases for CS2 consolidated samples and increases for CS1, achieving values up to 60 % respect Cu.

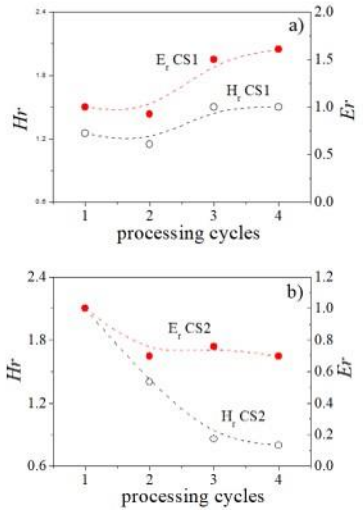

Fig. 18 Measured values for hardness (Hr) and elastic modulus (Er) of consolidated samples CS1 and CS2 plotted as a function of the number of treatment cycles tests and shown on a relative scale: a) CS1 and b) CS2 [7].

The above-mentioned evidence definitely suggests that the progressive increase of the graphite content in CS2 powders and consolidated samples determines a softening of the Cu matrix. Vice versa, the constancy of graphite content in CS1 samples allows a significant hardening and stiffening. At least in part, this can be also explained by the attainment of a finer microstructure in CS1 consolidated samples, which seems to indicate the capability of lower graphite content of hindering grain growth.

Additional evidence from TEM observation helps clarifying the scenario.

Representative TEM micrographs of CS1 and CS2 consolidated samples are shown in Figs. 19c and 19d respectively. In both cases, the repeated BM and SPS stages finally result in the formation of highly homogeneous microstructures. Severe mechanical deformation induces the formation of graphite nanoparticles approximately ranging between 5 to 8 nm in size.

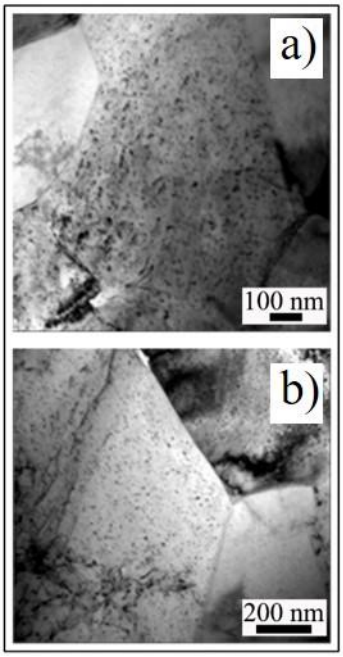

Fig. 19 Representative BF-TEM micrographs showing the microstructure of the a) CS1 consolidated samples and b) CS2 consolidated samples.

Invariably, nanoparticles are uniformly dispersed into the Cu matrix. Thus, the attainment of a uniform dispersion is independent of the total content of graphite. Quite reasonably, larger contents of graphite result in higher volume densities of graphite nanoparticles into the matrix.

Nevertheless, the total content of graphite has a clear effect on the distribution of graphite nanoparticles within the Cu matrix. Indeed, CS2 consolidated samples tend to exhibit preferential accumulation of graphite nanoparticles at grain boundaries. In contrast, CS1 consolidated samples have graphite nanoparticles spanning evenly from the grain interior to the grain boundary.

So small graphite nanoparticles seems that their properties can be expected to almost equate those of multilayer graphene [5].

TEM micrographs of CS1 consolidated samples at different magnification are reported in Figure 20.

As evident from Figs. 20c and 20d, the small graphite nanoparticles are able to hinder dislocation gliding and give rise to dislocation arrays. This effect, also, involves <111>, <220> and <200> crystallographic planes, which are the fundamental plane in face-centered cubic metals such as Cu. It follows that graphite nanoparticles contribute to the strengthening and stiffening of the Cu matrix.

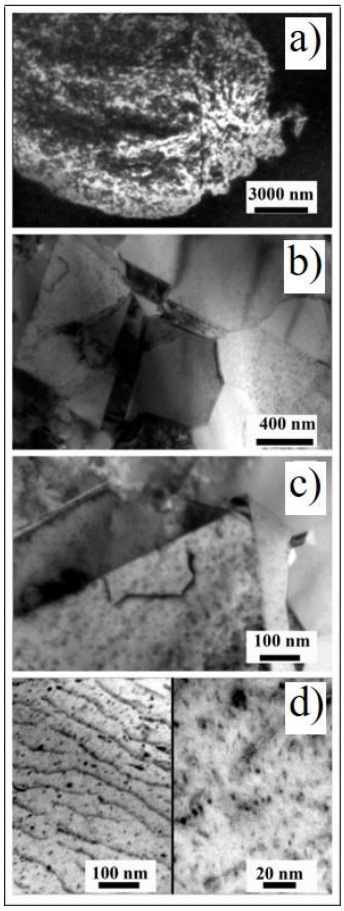

Fig. 20 TEM micrographs of CS1 at the fourth processing stage (a) a composite powder particle and of the microstructure of consolidated samples at lower (b) and higher (c) magnification showing twinning in Cu matrix and the uniform dispersion of graphite nanoparticles. (d) Details of dislocation arrays (left panel) and graphite nanoparticles (right panel) in consolidated samples [7].

Although the relatively high intrinsic mechanical strength of graphite nanoparticles provides an effective barrier against dislocation motion, the observed strengthening cannot be exclusively ascribed to dispersed graphite nanoparticles. The repeated severe plastic deformation of Cu and graphite can be reasonably expected to result in the gradual dissolution of very small C atom clusters, and even individual C atoms, in the metal matrix. Therefore, strengthening can be partially explained in terms of solid solution strengthening. In addition, the mechanical processing determines a relatively high content of twins in the Cu matrix, which also contribute to strengthening.

Further investigations on the mechanical properties through nanoindentation to determine the strain rate sensitivity of the Cu-C 3 wt.% CS1 samples in the four stages of treatments have been carried out.

5.1.3 Indentation strain rate sensitivity (SRS) study of the Cu-MCs with nano graphite

The MMC strain rate sensitivity (SRS) is an important parameter, which controls the metal ductility properties. High values of work hardening and SRS help to delay the onset of localized deformation under tensile stress, resulting in improved ductility [8].
Nanoindentation made it possible the systematic study of the time-dependent mechanical response by analysing the indentation load-displacement (P-h) curves without the need for hardness impression observation [9]. To this purpose, nanoindentation constant-load room-temperature creep experiments with a sharp Berkovich tip can be used [10–12].
A constant load method (Pmax = 10 mN) for an extended dwell time (5< td< 300 s) was used. From the depth increase, the continuous change in the stress during holding is thus evaluated.
With this respect, the continuous stress variation is estimated and then calculated from the hardness H measurements, through the Tabor's empirical law [13] $\sigma = H/C$, where C = 3 for metals. The indentation strain rate is calculated by $\varepsilon i = (dh/dt) h^{-1}1$. In order to directly compared the nanoindentation strain rate, εi, with conventional uniaxial creep strain rate, εu, the empirical relationship $\varepsilon u = 0.01\varepsilon i$ can be applied for the nanoindentation analyses [14].
In Figure 21 are reported the hardness values in function of td and in terms of the different strain rates, ε, for the four stages of BM/SPS treatments. A saturation value of the mean H was reached for td > 120s, in all the stages, that is essentially irrespective of the strain rate. In particular, H tends to stabilize at 0.35 GPa for Stage 1 and 2, while the H values distribution appeared more scattered. The average of H was higher in stage 3 (in the range of 0.75-1.5 GPa), to stabilize at the value of H about 1.0 GPa, in Stage 4 (H = 0.9-1.1 GPa).

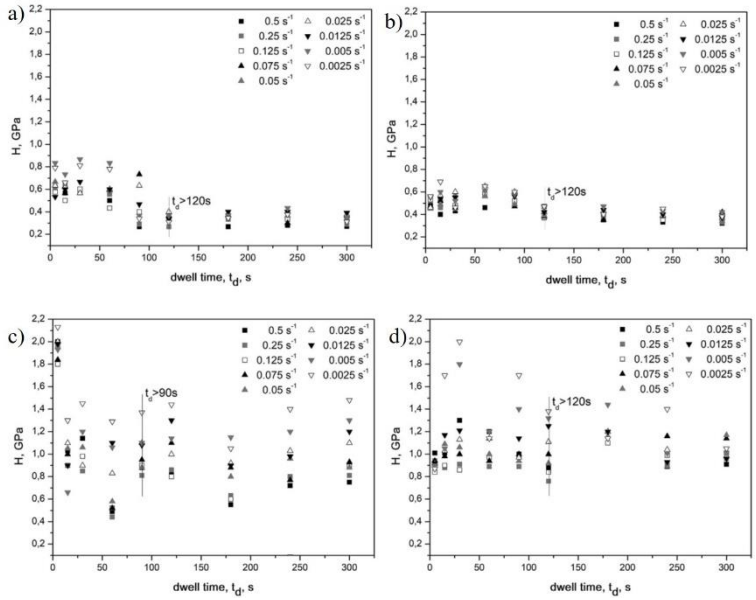

Fig. 21 H vs. dwell time, t_d, for the different strain rates ε = 0.0025-0.5 s^{-1}; BM/SPS compaction a) stage 1, b) stage 2, c) stage 3 and d) stage 4 [15].

Similar studies on magnesium-graphite reinforced MMC reported a significant increment of compressive strength, due to graphite particle acting as barriers to the sliding dislocations. It was shown that an increment of the graphite content, within the matrix, resulted in a significant increase of the alloy ductility, tensile strength, compressive strength, and Young's modulus, but a decrease of the hardness [16].

Therefore, a maximum hardness of about 70 HV for 1 vol % graphite reinforced by conventional sintering process, they reported. In the case of SPS treatment the hardness was reported to reach values up to100 HV, due to the good bonding strength between matrix and the reinforcements in the consolidate MMC [16]. Other researchers reported similar findings for Cu-C MCs [17–20].

In the present study, the hardness results obtained on Cu-C 3 wt.% with different BM/SPS stages are in good agreement with the research works found in literature.

The indentation creep rate, for a Berkovich tip, was calculated following the equation:

$$\varepsilon = \frac{dh/h}{dt} = \frac{h}{h'}$$

Where h is the displacement rate of the tip, and h’ is the instantaneous indenter displacement.

During the indentation test, the stress-strain fields below the tip change continuously and this region undergoes a creep strain after a long period.
Considering this, the penetration depth displacement (hc) graphs, where hc is plotted as a function of td, allow to determine the steady-state regimes for all the BM/SPS stages. The plots are shown in Figure 22.

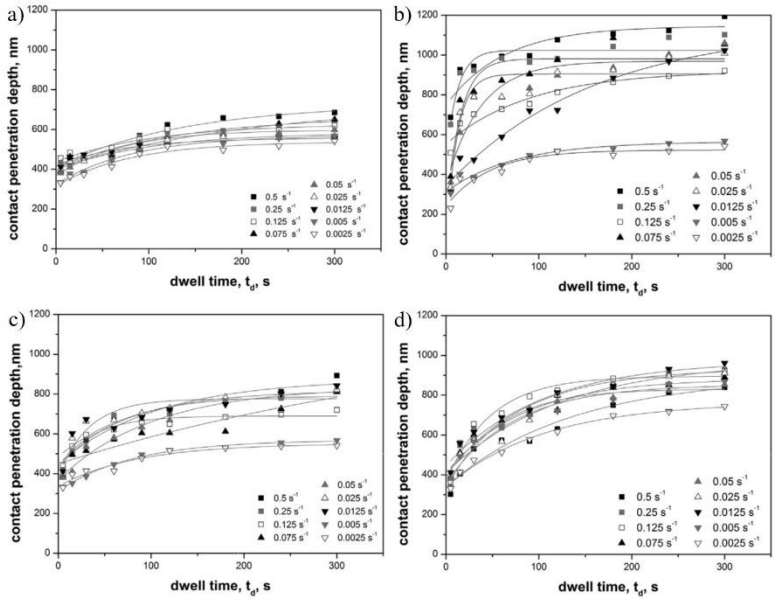

Fig. 22 Contact penetration depth, hc, vs. dwell time, td, for the different strain rates. ε = 0.0025-0.5s^{-1}; BM/SPS compaction a) stage 1, b) Stage 2, c) Stage 3, d) Stage 4 [15].

It was found that the secondary creep, with hc approximately constant, was attained early, for td > 120s, for all the four stages, and irrespectively of the strain rate. For short td, the creep strain was almost of primary type. As the stress induced by indentation at Pmax = 10mN was significantly high, the onset of secondary creep was expected to be fast.
The plots relative to the yield strength, σ, vs. the contact penetration depth, hc, for the four stage of BM/SPS treatments are shown in Figure 23. It can be noticed a significant difference between stages 1 and 2 and between stage 3 and 4. In particular, σ varied either with hc and ε. This variation ranged from 100 to 300 MPa in stage 1, reducing the maximum to 200 MPa in stage 2. The variation of σ in stage 3 and 4 was large, with high values, between 200 and 600 MPa, in the first and from 300 and 600 MPa in the second. At the same time, the maximum of penetration depth, in the different BM/SPS stages of treatment, reached a value of 900-1100 nm. The Cu-C Stage 3 appeared to be more scattered with a significant strength variation of Δσ = 500 MPa.

Considering the width of penetration depth, in stage 1 was 300-700 nm, in stage 2 was 300-1100 nm, in stage 3 was 300-800 nm and in Stage 4 was 300-900 nm.

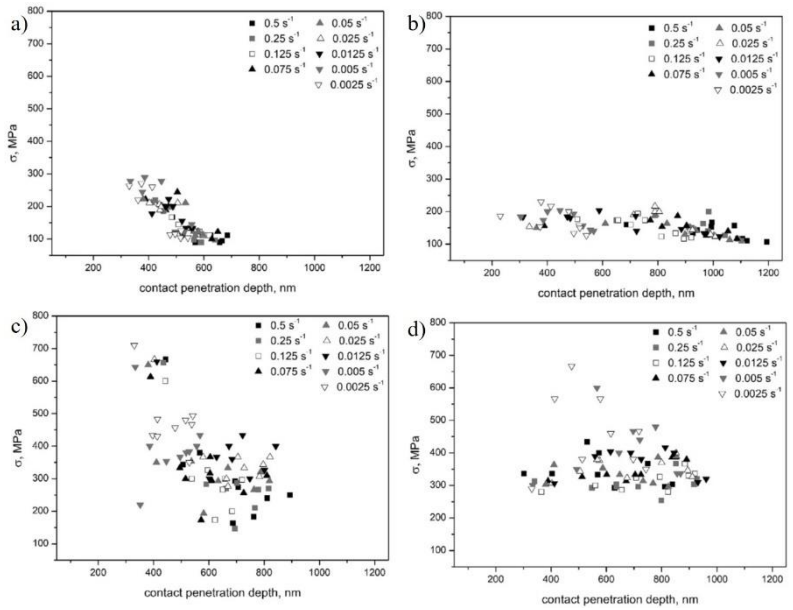

Fig. 23 Yield strength, σ, vs. contact penetration depth, hc, for the different strain rates ε = 0.0025-to-0.5s^{-1}; BM/SPS compaction a) Stage 1, b) Stage 2, c) Stage 3, d) Stage 4 [15].

The evaluation of SRS exponent, m, is plotted in Figure 24.

This parameter is calculated in the steady-state regime, in this case at td > 120s. It can be observed, in the figure, that the value of m is negative for all the four experimental conditions. The negative values of m are similar for stage 1 and stage 2, m is twice at stage 3, and it slightly decreases at stage 4.

The absolute values of m ranged between 0.039 and 0.076. These values are in accordance with the results found in literature for nanocrystalline Al and Pmax = 8 mN. This result together with the here reported are higher by an order of magnitude respect to 0.004 referred to a coarse grained Al [21]. This comparison suggest that the grain and the cell structure here reported are likely to be submicrometric. The microstructure TEM observation, reported hereafter, confirms this scale of the microstructure grain and cell structure.

To better understand the microstructure dependency on the SRS exponent, m, the approach suggested by the literature is to plot ln(H) vs. ln(td) at constant temperature and showing that the slope of the curve is $-\frac{1}{n}$ [22]. This relationship has been found to be very useful to study the indentation creep parameters for various structural materials [23].

In this case, the steady-state creep stress exponent n, was found to be in the range of 13-28. For stage 1 this parameter is n= 26. for stage 2 is n = 28, for stage 3 is n = 13 and for stage 4 is n = 19. These values are probably due to the presence of a high density of grain and cell boundaries. Low-angle (cells) as well as high-angle boundaries (grains) act as source and sink for the sliding and tangled dislocations. In fact, a high rate of generated dislocations (both sliding and tangled) would result in a high work hardening rate and consequently to high values of n.

The here obtained high values of n are also in agreement with previous researches, for instance, for nanocrystal Al [24].

High values of SRS values obtained from nanoindentation analysis indicate a good ductility of nanocrystalline metals qualitatively. However, elevated SRS values in nanocrystalline metals help to reduce plastic instability. This fact is probably due to the hardening of localized plastic deformation regions [25]. Thus, nano-sized twins crystals generally enhance the SRS of Cu alloys and Cu-graphite MMC [25–27].

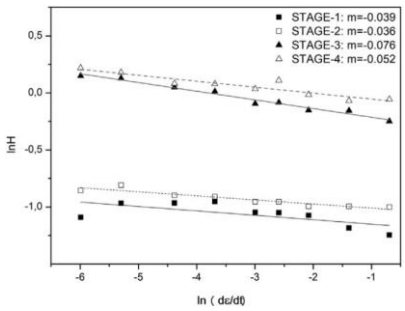

Fig. 24. Evaluation of the SRS exponent m for the four Stages 1-to-4, in the material) steady-state regime (i.e., for td > 120s, as determined by the plot of Figs. 1 and 2) [15].

In Figure 25 are reported the TEM micrographs of Cu-C 3 wt.% at the different stages from 1 to 4 of BM/SPS treatments. The microstructure, as it can be seen in figure, seems to slowly evolve towards smaller cell sizes with the increasing of the treatments. At the same time, the grained structure seems to be less influenced by the treatments. However, the density of low angle boundary tends to slightly increase with the BM/SPS treatments. The average dimension of cell result in 450 nm in stage 1, in 300 nm in stage 2, in 340 nm in stage 3 and in 280 nm in stage 4. The mean grain size remained essentially insensitive to the progressive BM/SPS treatments. Instead the progressive BM/SPS treatments rather influenced the dissolution of graphite in the Cu matrix. The size of C

agglomeration within the Cu grain seems to be less than 5 nm and it tended to increase with the BM/SPS treatments.

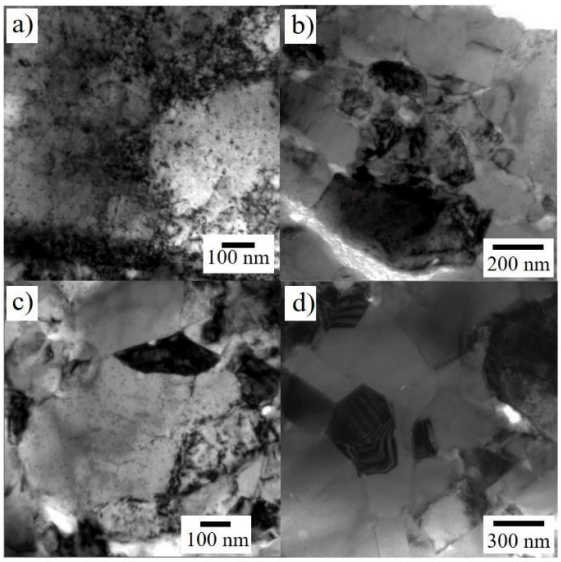

Fig. 25 TEM micrographs showing the grain and cell structure formed by the BM/SPS at different compaction stages a) stage 1, b) stage 2, c) stage 3 and d) stage 4 in the Cu-C 3 wt.% [15].

The plot of the SRS values as a function of the inverse of the mean hardness is shown in Figure 26. It can be seen, in figure, a linear interpolation of the experimental and calculated data. The linearity between the SRS exponent m and H^{-1} is attended because m can be expressed as

$$m=\frac{kT}{V\tau}$$

where k is the Boltzmann constant, T is the temperature in Kelvin, V is the activation volume associated with the plastic deformation induced by the nanoindentation measurements, and τ is the applied shear stress [59]. Considering a Taylor factor equal to 3, and the Tabor's factor being 3, the hardness H = 9 τ.

The plot of Fig. 26 refers to m values which derived from contact penetration depths, hc > 500 nm, and dwelling times, td > 120s, where a steady-state regime is reached. The existing relationship between the SRS exponent, m, and the mechanical response of the material, H, deducted by nanoindentation method, is expected to be inversely proportional. This mainly due to the activation volume V, during the nanoindentation

penetration depth, using a pyramidal Berkovich tip, that is actually related to the creep steady state regime.

This relationship, calculated by linear interpolation, was: m = - 0:037H^{-1} - 0:021 for td > 120s. in Figure 26 the datapoints referring to stage 1 and 2 are close to the curve instead datapoints of stage 3 and 4 are far. The interpolation indicates a reasonable linearity between m and H^{-1}. It is also worth noting that the SRS exponents of stages 1 and 2 have a double value compared to what obtained for stage 3, and they are higher by 50% compared to what obtained for stage 4. This can be related to microstructure features that differentiated the stages 1 and 2 from the stage 3, and possibly the stage 4.

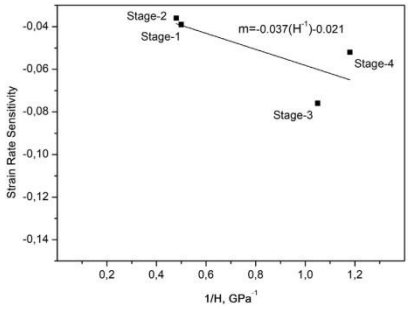

Fig. 26 SRS vs. H^{-1}, where H refers to the mean hardness value obtained at each Stage. On the basis of the existing relationship between m and the applied shear stress, τ, the linear interpolation allows to determine a mean linearity factor, between Stages 1 and 2, and Stages 3 and 4, of -0.0037 [15].

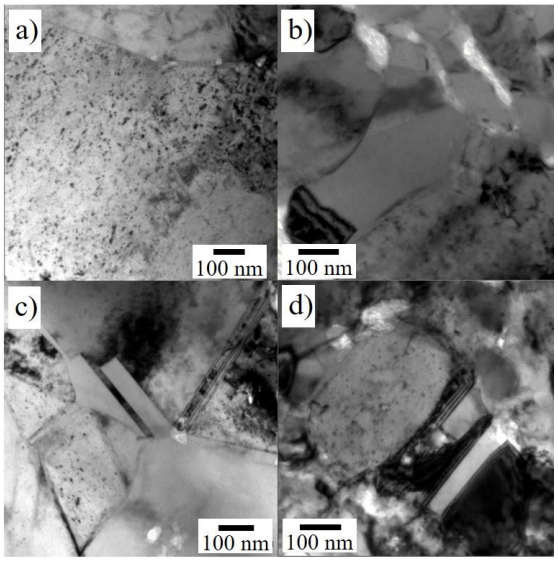

Fig. 27 TEM representative micrographs showing Cu grain twinning induced by the BM/SPS different compaction level a) stage 1, b) stage 2, c) stage 3 and d) stage 4 [15].

In Figure 27, are shown the TEM micrographs regarding the Cu grain twinning.
The figure shows some correlation between the density of Cu-grain twinning and the SRS exponents here obtained for Stages 1-to-4. The volume fraction of twinning in the Cu grain interior tends to increase as the SRS exponent m decreases. A larger fraction of twinning was found in stage 3 where m= 0.076, while significantly minor in the other stages.

5.2 Synthesis of Cu-MCs reinforced with Graphene by MLM: a bottom-up approach

The preparation of the Cu-Graphene composite powders occurs through the redox synthesis and precipitation of the Cu powder. During the reduction reaction of the Cu precursor and the precipitation of the powder the incorporation of graphene into the matrix takes place.
By selecting the precursors, various syntheses were performed with different pH or compositions between the precursors. The final goal was to achieve an optimal dispersion of graphene into the matrix, the production of Cu powder without the presence of oxides, a good quantity of products and a simple procedure of reaction.
Here it is explained the selected redox synthesis, that is an optimal procedure for the production of about 1 g of powder of Cu in four hours at low temperature.

Fig. 28 Redox synthesis of Cu powder: evolution of the reaction over the 4 hours of stirring at 60°C.

The evolution of the redox reaction is shown in Figure 28.

The reaction starts with the dispersion of the precursor Cu chloride, that has been mixed with the ascorbic acid and, during the reduction of Cu^{2+} to Cu^{0}, take place the synthesis of the Cu powder that precipitate as a red powder. During the first part of the synthesis, in the stage of the preparation of the two solutions, a diluted solution of graphene has been dispersed, in this way during the precipitation of Cu the dispersoid can be incorporated into the matrix.

Three batches of powder samples, through this synthesis, were prepared Cu, Cu-graphene 0.3 wt.% and Cu-graphene 1 wt.%.

The composite powders were characterised by SEM microscopy and XRD.

The micrographs of Cu-graphene 0.3 wt.% in comparison with Cu powders are shown in Figure 29.

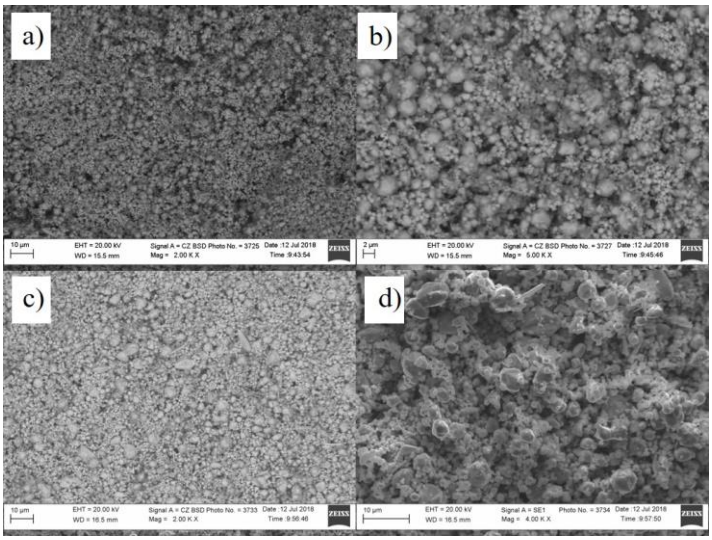

Fig. 29 SEM micrographs of the synthesized powders at various magnifications: a) and b) Cu c) and d) and Cu-graphene 0.3 wt.%.

In Figures 29 a and b, it can be noticed that, Cu powders are constituted to small particles of about 0.5-1 µm and larger aggregates of 2-3 µm. While, in Figure 29 b and c, relative to the Cu-graphene 0.3 wt.% composite powders are composed to small particles of 0.5-1 µm, aggregates of 2-3 µm and larger and more elongated parts of 0.22*2 µm. A detail of the Cu-graphene 0.3 wt.% microstructure is reported in Figure 30.

The micrographs of Cu-graphene 1 wt. % in comparison with that related to Cu powders, are shown in Figure 31. In this case, the composite powders show a distribution of a small quantity of particles of 1 µm and higher amount of large aggregates of 6-13 µm.

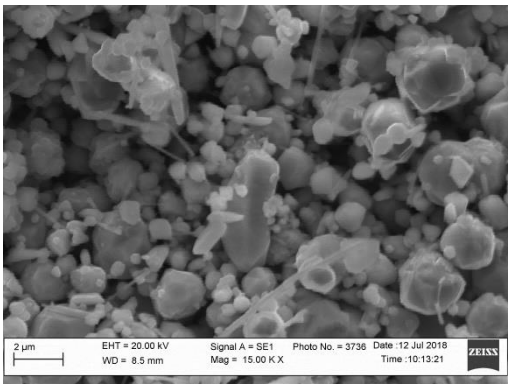

Fig. 30 SEM micrography of Cu-graphene 0.3 wt.% composite powder at 15000 X of magnification.

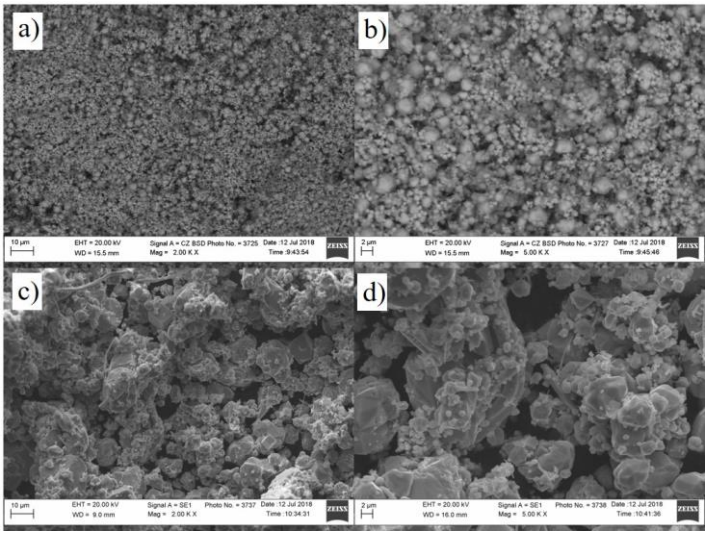

Fig. 31 SEM micrographs of the synthesized powders at various magnifications: a) and b) Cu c) and d) and Cu-graphene 1 wt.%.

The powders of Cu, Cu-graphene 0.3 wt.% and Cu-Graphene 1 wt.% were consolidated through SPS at 900 °C for 10 min. Then the powders and the consolidated samples were characterised by XRD.

The XRD patterns of Cu, Cu-graphene 0.3 wt.% and Cu-graphene 1 wt.% powders and consolidated samples are shown in Figure 32.

In the figures, it can be noticed that all the produced powders and consolidated samples exhibit the peaks of Cu cubic phase. There are small differences between intensity and width of the peaks. In particular, it can be noticed that, in the case of the consolidated samples there is a shift to high angle of the XRD patterns.

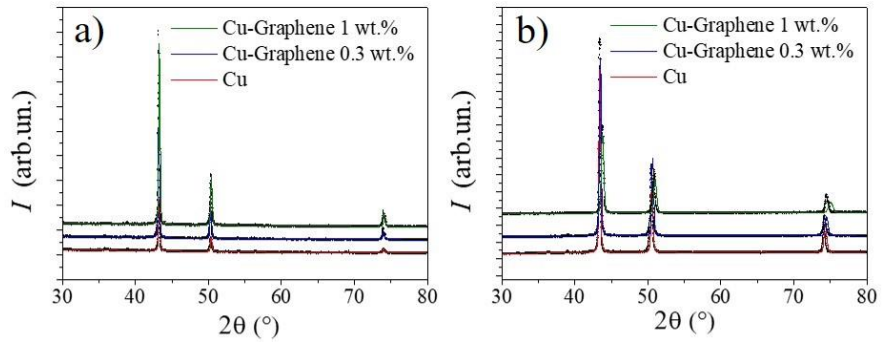

Fig. 32 XRD patterns of Cu and composites a) powders and b) consolidated samples at 900°C for 10 min.

The geometrical densities of the Cu, Cu-graphene 0.3 wt.% and Cu-graphene 1 wt.% consolidated samples were evaluated.

In Table 12 are reported the geometric densities of the consolidated samples in comparison with the theoretical mixture values. In the table it can be noticed that the addition of 0.3 wt.% of graphene to the matrix doesn't affect the density, while, on the contrary, when it is added up to 1wt.% the density increased.

Tab. 12 Densities values of the composite sample in comparison with Cu.

Sample	**ϱ mix**	**ϱ geometrical**	**relative density %**
Cu	8.96	8.194	91.4
Cu-Graph 0.3 wt.%	8.88	8.091	91.1
Cu-Graph 1 wt. %	8.69	8.39	96.6

The Rietveld analysis results of the Cu, Cu-graphene 0.3 wt.% and Cu-graphene 1 wt.% are shown in Table 13.

The addition of graphene to the synthesis of Cu increase the crystallite size up to 200 nm, over the limit detectable to the Rietveld refinement. The cell parameter in the case of 0.3 wt.% of graphene increases probably due to the incorporation of graphene into the cell. Instead in the case of Cu-C 1 wt.% the cell parameter doesn't change respect to Cu.

Tab. 13 XRD Rietveld refinement results for the Cu and Cu-graphene 0.3 wt.% and Cu-graphene 1 wt.% samples powders.

Powder sample	Cell parameter (Å)	Crystallite Size (nm)	Microstrain	Texture	Rwp
Cu	3.620	156.9	$4.5*10^{-4}$	*	8.9
Cu – Graph 0.3 %	3.625	>200	$5.7*10^{-4}$	*	12
Cu – Graph 1 %	3.619	>200	$6.1*10^{-4}$	*	8.9

In Table 14 are reported the XRD refinement of the Cu, Cu-graphene 0.3 wt.% and Cu-graphene 1 wt.% consolidated samples at 900°C.

In that case, the consolidation treatment to the powders reduced, for all the cases the cell parameters but has small influence to the crystallite size that is up to the limit of detectability of the Rietveld analysis.

Tab. 14 XRD Rietveld refinement results of Cu, Cu-graphene 0.3 wt.% and Cu-graphene 1 wt.% consolidated samples with SPS at 900°C for 10 min.

Consolidated sample SPS 900°C 9 + 10 min	Cell parameter (Å)	Crystallite Size (nm)	Microstrain	Texture	Rwp
Cu	3.609	145.5	0.001	*	14.9
Cu – Graph 0.3 %	3.602	>200	0.001	*	15.3
Cu – Graph 1 %	3.579	>200	0.003	*	22.2

The consolidated samples with the three different compositions were tested to determine hardness and elastic modulus by nanoindentation. The hardness and elastic modulus of the consolidated samples are shown in Figure 33. It can be seen that increasing the content of graphene in the samples affects positively the two quantities.

TEM observation of the composite with 0.3 wt.% and 1 wt.% of graphene are shown in Figure 33 and 34 respectively. As it can be seen in figure, after the synthesis and consolidation for the two compositions graphene is homogeneous distributed into the matrix of Cu. The dispersion of the dispersoid results distributed at a molecular level.

Comparing the Figures 34 and 35, it can be noticed that, obviously, the average dimensions and the quantity of carbon in the case of 0.3 wt.% are slightly minor than what observed for the sample with 1 wt.%.

Observing the figures, in case of 0.3 wt.% the dimension of graphene into the matrix are minor than 4 nm, while for 1 wt.% are greater than 5 nm.

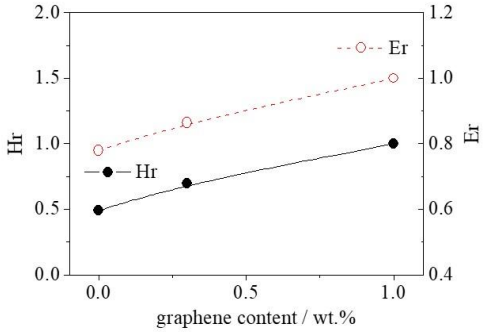

Fig. 33 Measured values of hardness (Hr) and elastic modulus (Er) of consolidated samples of Cu-graphene as a function of the content of graphene (0, 0.3 and 1 wt.%).

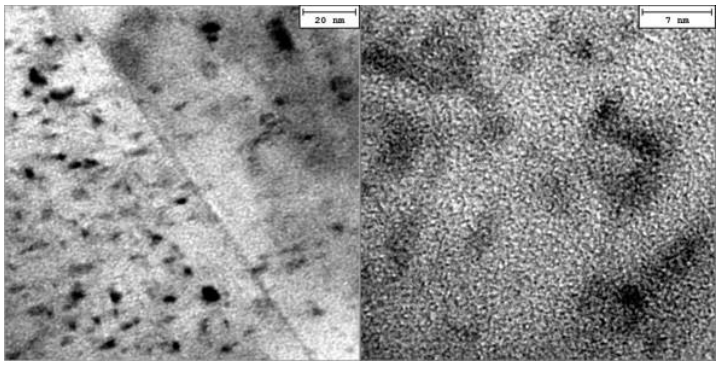

Fig. 34 TEM observation of Cu-graphene 0.3 wt.% consolidated sample.

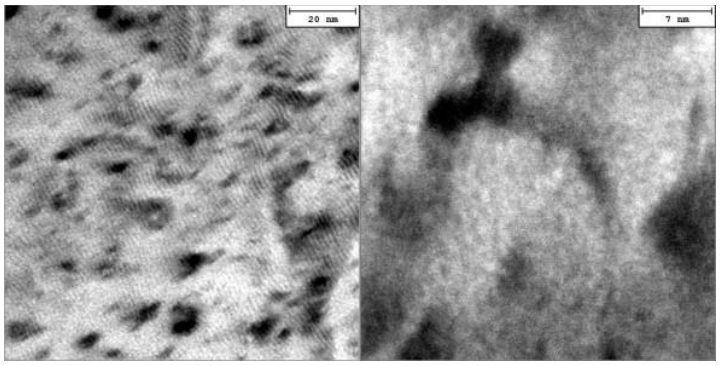

Fig. 35 TEM observation of Cu-graphene 1 wt.% consolidated sample.

Bibliography

[1] Jing-fu LI, Sliding wear behavior of copper-based composites reinforced with graphene nanosheets and graphite, Trans. Nonferrous Met. Soc. China. 25 (2015) 3354−3362.

[2] N. G. A. Antonelli, S. Reddy, P. Subramonium, J. Henri, J. Sims, J. O'loughlin, and H.S. Shamma, D. Schlosser, T. Mountsier, W. Guo, Patterning with Amorphous Carbon Thin Films, ECS Trans. 35 (2011) 701. doi:10.13140/2.1.4619.9684.

[3] M.A. Pimenta, G. Dresselhaus, M.S. Dresselhaus, L.G. Cançado, A. Jorio, R. Saito, Studying disorder in graphite-based systems by Raman spectroscopy, Phys. Chem. Chem. Phys. 9 (2007) 1276–1291. doi:10.1039/b613962k.

[4] M. Hasegawa, K. Sugawara, R. Suto, S. Sambonsuge, Y. Teraoka, A. Yoshigoe, S. Filimonov, H. Fukidome, M. Suemitsu, In Situ SR-XPS Observation of Ni-Assisted Low-Temperature Formation of Epitaxial Graphene on 3C-SiC/Si, Nanoscale Res. Lett. 10 (2015). doi:10.1186/s11671-015-1131-9.

[5] P. Wick, A.E. Louw-Gaume, M. Kucki, H.F. Krug, K. Kostarelos, B. Fadeel, K.A. Dawson, A. Salvati, E. Vázquez, L. Ballerini, M. Tretiach, F. Benfenati, E. Flahaut, L. Gauthier, M. Prato, A. Bianco, Classification framework for graphene-based materials, Angew. Chemie - Int. Ed. 53 (2014) 7714–7718. doi:10.1002/anie.201403335.

[6] A. Bianco, H.M. Cheng, T. Enoki, Y. Gogotsi, R.H. Hurt, N. Koratkar, T. Kyotani, M. Monthioux, C.R. Park, J.M.D. Tascon, J. Zhang, All in the graphene family - A recommended nomenclature for two-dimensional carbon materials, Carbon N. Y. 65 (2013) 1–6. doi:10.1016/j.carbon.2013.08.038.

[7] B. Lasio, F. Torre, R. Orrù, G. Cao, M. Cabibbo, F. Delogu, Fabrication of Cu-graphite metal matrix composites by ball milling and spark plasma sintering, Mater. Lett. 230 (2018) 199–202. doi:10.1016/j.matlet.2018.07.120.

[8] Y.T. Zhu, X. Liao, Nanostructured metals: retaining ductility., Nat. Mater. 3 (2004) 351–352.

[9] W.H. Poisl, W.C. Oliver, B.D. Fabes, The relationship between indentation and uniaxial creep in amorphous selenium, J. Mater. Res. 10 (1995) 2024–2032. doi:10.1557/JMR.1995.2024.

[10] R. Goodall, T.W. Clyne, A critical appraisal of the extraction of creep parameters from nanoindentation data obtained at room temperature, Acta Mater. 54 (2006) 5489–5499. doi:10.1016/j.actamat.2006.07.020.

[11] C.L. Wang, Y.H. Lai, J.C. Huang, T.G. Nieh, Creep of nanocrystalline nickel: A direct comparison between uniaxial and nanoindentation creep, Scr. Mater. 62 (2010) 175–178. doi:10.1016/j.scriptamat.2009.10.021.

[12] Z.S. Ma, S.G. Long, Y.C. Zhou, Y. Pan, Indentation scale dependence of tip-in creep behavior in Ni thin films, Scr. Mater. 59 (2008) 195–198. doi:10.1016/j.scriptamat.2008.03.014.

[13] D. Tabor, The hardness and the strength of metals, J. Inst. Met. 79 (1951) 1–18.

[14] C.L. Wang, M. Zhang, T.G. Nieh, Nanoindentation creep of nanocrystalline nickel at elevated temperatures, J. Phys. D. Appl. Phys. 42 (2009). doi:10.1088/0022-3727/42/11/115405.

[15] M. Cabibbo, C. Paoletti, B. Lasio, R. Orrù, F. Delogu, Indentation strain rate sensitivity of ball-milled spark-plasma sintered Cu-C metal matrix composite, J. Alloys Compd. 767 (2018) 838–847. doi:10.1016/j.jallcom.2018.07.155.

[16] Seah, K H W, Sharma, Satish C., G. B.m., Development and performance analysis of novel cast copper-SiC-Gr hybrid composites, Mater Des. 16 (1995) 271–275.

[17] C.S. Ramesh, R. Noor Ahmed, M.A. Mujeebu, M.Z. Abdullah, Development and performance analysis of novel cast copper-SiC-Gr hybrid composites, Mater. Des. 30 (2009) 1957–1965. doi:10.1016/j.matdes.2008.09.005.

[18] K. Rajkumar, S. Aravindan, Microwave sintering of copper-graphite composites, J. Mater. Process. Technol. 209 (2009) 5601–5605. doi:10.1016/j.jmatprotec.2009.05.017.

[19] A. Yeoh, C. Persad, Z. Eliezer, Dimensional responses of copper-graphite powder composites to sintering, Scr. Mater. 37 (1997) 271–277. doi:10.1016/S1359-6462(97)00114-0.

[20] R.K. Gautam, S. Ray, S.C. Sharma, S.C. Jain, R. Tyagi, Dry sliding wear behavior of hot forged and annealed Cu-Cr-graphite in-situ composites, Wear. 271 (2011) 658–664. doi:10.1016/j.wear.2010.11.033.

[21] J. May, H.W. Höppel, M. Göken, Strain rate sensitivity of ultrafine-grained aluminium processed by severe plastic deformation, Scr. Mater. 53 (2005) 189–194. doi:10.1016/j.scriptamat.2005.03.043.

[22] P.M. Sargent, M.F. Ashby, Indentation creep, Mater. Sci. Technol. 8 (1992) 594–

601.

[23] G. Sharma, R. V. Ramanujan, T.R.G. Kutty, N. Prabhu, Indentation creep studies of iron aluminide intermetallic alloy, Intermetallics. 13 (2005) 47–53. doi:10.1016/j.intermet.2004.05.008.

[24] S. Varam, K. V. Rajulapati, K. Bhanu Sankara Rao, Strain rate sensitivity studies on bulk nanocrystalline aluminium by nanoindentation, J. Alloys Compd. 585 (2014) 795–799. doi:10.1016/j.jallcom.2013.09.116.

[25] Q. Wei, Strain rate effects in the ultrafine grain and nanocrystalline regimes-influence on some constitutive responses, J. Mater. Sci. 42 (2007) 1709–1727. doi:10.1007/s10853-006-0700-9.

[26] X.Z. Liao, F. Zhou, E.J. Lavernia, D.W. He, Y.T. Zhu, Deformation twins in nanocrystalline Al, Appl. Phys. Lett. 83 (2003) 5062–5064. doi:10.1063/1.1633975.

[27] M. Chen, E. Ma, K.J. Hemker, H. Sheng, Y. Wang, X. Cheng, Deformation twinning in nanocrystalline aluminum, Science (80-.). 300 (2003) 1275–1277. doi:10.1126/science.1083727.

6. Conclusions

- The systematic series of experiments performed in the first part of the thesis has permitted determining the optimal operative conditions, in order to achieve the fabrication of Cu-MC reinforced with graphite with good mechanical properties. The XRD, nanoindentation and SEM characterisation techniques have allowed to identify the composition of the composite and the advantageous conditions for the fabrication. The composite Cu-C 3 wt.% that was prepared with 24 hours of milling and consolidated at 900°C achieved good mechanical properties compared to the other published results. The dispersion of the reinforcement into the matrix obtained by ball milling and the subsequently SPS consolidation resulted in the fabrication of a composite with good mechanical properties and a lamellar microstructure.
- The promising methodology of fabrication has been improved to achieve a homogeneous dispersion of the reinforcements at the atomic level and consequently led to enhancing the mechanical properties of the composite. Then, a novel methodology with consecutive steps was defined through the combined use of BM and SPS. The combination of BM and SPS allowed to disperse uniformly graphite nanoparticles into the Cu matrix and to incorporate through the growth of the Cu grains. The influence of graphite nanoparticles on the mechanical properties of the Cu-C depends on the total amount of dispersed graphite. A significant hardening and stiffening of the Cu-C containing only 3 wt.% of graphite is observed as the number of treatment cycles increases, while the progressive addition of graphite depresses the mechanical properties. The enhanced mechanical properties of the Cu matrix can be ascribed to a combination of solid solution and twinning strengthening mechanisms.
- The study of the room temperature creep and the strain rate sensitivity (SRS) of Cu-C 3 wt.% through nanoindentation technique have provided interesting results. SRS exponent, m, in all the four BM/SPS stages was negative, and its absolute value was higher in the last two stages of treatments related to the first two. Qualitatively the high value of SRS indicates a good ductility of the bulk material. On the contrary the constant reduction of the SRS exponent means ductility degradation, as the processing stages increase. Moreover, larger variation of the

SRS exponent reveals a faster ductility variation. The steady-state exponent, n, was found to be in the range of 13 and 28; these values are due to the presence of grain and cell boundary. TEM micrographs revealed the correlation between the high values of steady state creep stress exponent, n, and the lower values of SRS exponent, m. higher values of n were found, which are due to a large fraction of cell (low-angle) boundary, while lower values are related to a large volume fraction of twinning within the Cu sub-micrometer grains.

- Another method of fabrication to disperse the reinforcement into the matrix of Cu has been tested. This method, through a bottom-up approach, allows to obtain a molecular level mixing of the constituents. During the redox synthesis to obtain of Cu powder, graphene was incorporated into the matrix of Cu. Two compositions of graphene have been tested to obtain composite powders and were characterised by XRD, SEM. Further, Cu and the composite powders were consolidated to obtain a bulk sample and were characterised by XRD, Nanoindentation and TEM.
- The reinforcement of Cu-MCs by graphite nanoparticles and graphene has shown their potential as alternatives to CRMs in technological materials. Graphite can be used as a carbon source and as a precursor of graphene derivatives. The results obtained on a lab scale can provide a good starting point to design innovative materials with a reduced content of CRMs.

List of publications

B. Lasio, F. Torre, R. Orrù, G. Cao, M Cabibbo, F. Delogu, Fabrication of Cu-graphite metal matrix composites by ball milling and spark plasma sintering. Materials Letters 230 (2018) 199-202.

M. Cabibbo, C. Paoletti, B. Lasio, R. Orrù, F. Delogu, Indentation strain rate sensitivity of ball-milled spark-plasma sintered Cu-C metal matrix composite. Journal of Alloys and Compounds 767 (2018) 838-847.

B. Lasio, G. Pia, S. Garroni, R. Orrù, L. Takacs, F. Delogu, Non-monotonic variation of the grain size in Cu nanopowders subjected to ball milling. Materials Letters 212 (2018) 171-173.

List of Conferences

Workshop Premi "Gianni Licheri", Department of Chemistry, Cagliari 22 June 2018, Poster presentation: Fabrication of Cu-graphite metal matrix composites.

4th International Workshop on Spark Plasma Sintering, Cagliari 23- May 2018.

E MRS Fall 2017 Varsaw Poland 18-20 September 2017, Poster presentation: Mechanical Processing of Cu-graphite powders mixtures and subsequent consolidation.

INCOME 2017 Kosice Slovack 4-6 September 2017, Poster presentation: Fabrication of Cu-graphite metal matrix composites.

International Spring school on forefront alloys and advanced materials for extreme conditions «Icarus and Supermat», Chia (CA), 15-17 May 2017.

Seminar "The history of mechanochemistry" Prof. L. Takacs, Department of Chemistry Sassari, 20 January 2017.

Acknowledgements

I am sincerely grateful to my supervisor, Prof. Francesco Delogu, for support and motivation along the way to this final reach.
I would like to thank Prof. Roberto Orrù and Prof. Giacomo Cao for the opportunity they gave me to make this experience and for the support and assistance during the PhD.
I would like to express all of my gratitude to Prof. Roberta Licheri for friendship and the constant help in the lab during the whole collaboration period.
Many thanks to Prof. Marcello Cabibbo for kindness and helpfulness in the mechanical and microscopical characterisation of samples.
I am grateful to Prof. Carlo Ricci for Raman measurements.
Prof. Paola Meloni and Dr. Gianfranco Carcangiu are gratefully acknowledged for XRD and SEM characterisations.
I would like to thank also professors, researchers, technicians and administration officers of the Department of Mechanical, Chemical and Materials Engineering for their kind availability.

Dear Amit and Ombretta, thank you very much for your invaluable help during the PhD.

A big thank to my colleagues, friends and lunch and coffee mates Prof. Roberta Licheri, Dr. Giorgio Pia, Dr. Luca Pilia, Dr. Elodia Musu, Dr. Ludovica Casnedi. It has been very nice to share with you the little spare time during my lab and writing activities.

Dr. Laura Mais, Dr. Marina Luginina, Dr. Francesco Torre, Dr. Selena Montinaro, Dr. Santina Soru, Dr. Luisa Mancuso, Dr. Clara Musa, Dr. Gabriele Traversari, Dr. Fabio Fanari, Dr. Blessing Ezealigo, Dr. Giovanna Tallarita, Dr. Giorgio Ligios, Dr. Alessandra Taris, Alessandro Soggiu… Thank you so much for your help during these three years: It has been a pleasure to meet you.

My deepest gratitude to Franco, to my family and to my friends for the ceaseless support during my entire life.